ARCHIVES OF MECHANICS
Arch. Mech. **73** (5–6), 421–470, 2021, DOI: 10.24423/aom.3726

Comparative FE-studies of interface behavior of granular Cosserat materials under constant pressure and constant volume conditions

B. EBRAHIMIAN[1)], M. I. ALSALEH[2)], A. KAHBASI[3)]

[1)] *Faculty of Civil, Water and Environmental Engineering, Shahid Beheshti University (SBU), Tehran, Iran, e-mails: b_ebrahimian@sbu.ac.ir, ebrahimian.babak@gmail.com (corresponding author)*

[2)] *R & D, Virtual Product Development Technology, Caterpillar Inc., Mossville, IL 61552, U.S.A.*

[3)] *Faculty of Civil, Water and Environmental Engineering, Shahid Beheshti University (SBU), Tehran, Iran*

This article shows the outcomes of a systematic series of finite element (FE) calculations relevant to the shear behavior of a particulate-continuum interface system under different normal boundary conditions. In this respect, shearing of a thin and long granular Cosserat layer in the vicinity of a rigid moving wall with varied surface roughness values is analyzed under constant normal pressure and constant volume conditions. The material behavior is defined with a special elasto-plastic Cosserat model, taking into account micro-rotation, micro-curvature, couple stress, and mean particle size. The interaction between the layer of boundary particles and the surface roughness of the adjoining bottom wall is modeled by the rotation resistance of particles along the wall surface. Herein, the coupled effects of normal confining constraints imposed on the layer and the surface roughness of the bottom wall, are considered on the response of granular material under shearing. The influences of pressure level and initial void ratio are explored as well. Numerical results demonstrate that the dilatancy constraint prescribed to the interface plane in the normal direction, and the wall roughness have visible influences on the interface shear resistance as well as the deformation field formed within the layer. After large shearing, the width of the localized zone along the wall does not necessarily depend on the normal confining constraint and the applied pressure level. However, the localized zone characteristics and the interface shear response are mainly affected by the initial void ratio of the material. In addition to FE analyses, DEM-based simulations are also performed to investigate the micro-mechanical response of granular medium adjacent to a wall under shearing. FE predictions are qualitatively compared with DEM results, and reasonable agreement is observed.

Key words: interface shearing, wall roughness, constant pressure, constant volume, dilatancy constraint, Cosserat FE model, discrete element method (DEM).

1. Introduction

Measuring interface shear resistance of granular materials is inherently a boundary value problem [1, 2]. It is experimentally evident that the boundary constraint imposed on the orientation normal to the common plane between soil medium and moving wall affects the interface behavior of soil-structure system [2–4]. In engineering practice, the boundary conditions perpendicular to the interface plane are originated from the stiffness of neighboring material (e.g., soil, rock, or structure) and can have multiple types from free to full constraint of dilatancy [1, 10, 11, 15]. The confinement of adjoining material can change the normal stresses applied on the wall surface, and accordingly, control the shear resistance along the interface. Herein, the normal stiffness is characterized by the ratio of normal stress variation to normal displacement variation (i.e., dilation or contraction) at the upper boundary of the granular layer. According to Fig. 1(a, b), it varies between zero and infinity in the interfaces under constant normal pressure (CP) and constant volume (CV) conditions, respectively. The former describes the condition that the normal pressure is constant during shear, and the granular body dilates or contracts freely, Fig. 1(a). However, no vertical movement is permitted at the upper boundary of the granular body in the latter condition, Fig. 1(b). This implies that a volume change is completely prevented in CV condition. For this reason, CV is also denoted as the constant height [3, 16]. During CV condition, the normal stresses at the interface increase or decrease based on the tendency of a granular material to dilate or contract. It is shown in experiments that the results of CP and CV interface shear tests are different in the context of volume change and mobilized stresses along the interface [6, 14]. They are recognized as the extreme direct interface shear paths [5, 6, 17].

The practical examples of interface shearing of soil under CV condition can be found in the vicinity of displacement piles, soil nails and ground anchors under driving and axial loading [5, 6, 12, 18, 19] or near pre-stressed reinforced soil structures [12, 20, 21].

Running truly CV interface shear test in the laboratory is rather difficult, as little volume change is frequently observed in the specimen due to the limited rigidity of reaction frame in the testing device against the specimen heaving and expansion. Subsequently, the changes in normal stresses applied to the interface during the CV shear test cannot easily be obtained [12]. Furthermore, the residual interface shear resistance can be measured when the specimen is subjected to large and preferably unlimited shear displacement [4, 6, 9–11]. However, most laboratory works have been carried out at small to moderate strains and do not allow a sufficient amount of continuous shearing to attain a residual state. In addition to all the above deficiencies, most previous experimental studies have

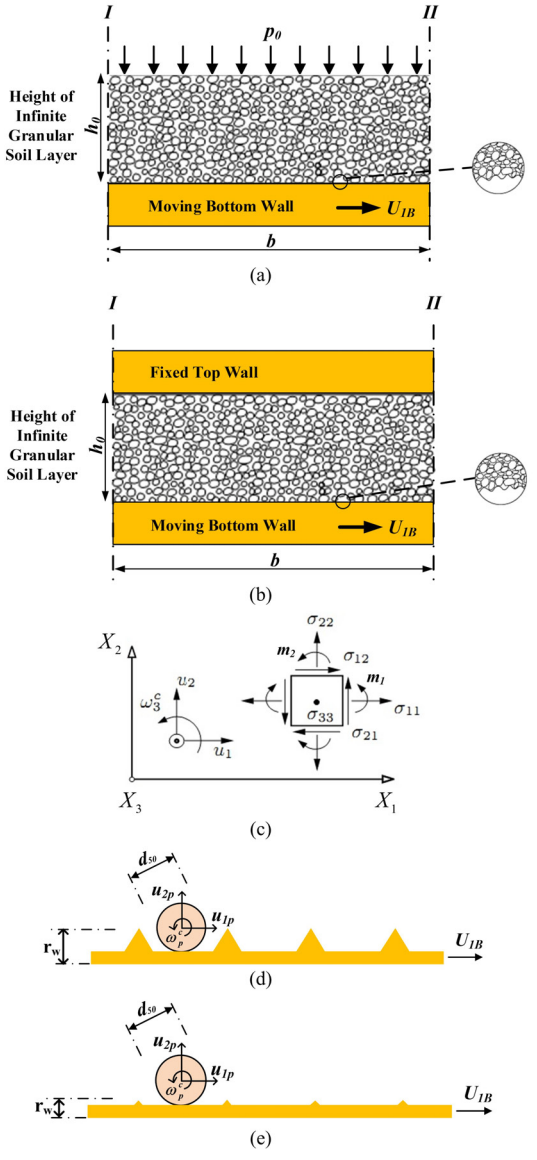

FIG. 1. Plane interface shearing of an infinite granular soil layer under: (a) constant pressure (CP) and free dilatancy, and (b) constant volume (CV) and constrained dilatancy; (c) kinematics and static quantities of Cosserat material under plane strain condition; kinematics along (d) rough and medium rough ($0 < r_w/d_{50} < 1$), and (e) relatively smooth ($r_w/d_{50} \approx 0$) walls.

mainly focused on exploring and measuring macro-scale quantities influencing peak and steady-state strength along the granular-continuum interfaces. They have not produced micro-scale information interior to the granular soil speci-

mens due to difficulties in quantifying and collecting microscopic data, at the scale of soil grains. Due to limitations, complexities, and difficulties related to performing CV interface shear tests in laboratory, numerical modeling at micro-level can be an efficient tool to more accurately explore the shear behavior of granular materials at interfaces under CV condition.

A limited number of experimental and numerical investigations has been carried out to study the shearing of granular bodies along interfaces under CV condition [1, 4–6, 8, 10–18, 20–27]. Except [1, 15, 25], the other mentioned numerical investigations have been performed within the framework of the classical continuum. Consequently, they cannot appropriately scale the width of the localized shear zone along the wall, as they have no intrinsic length scale within their formulations [5, 6, 16, 27, 28]. Moreover, the dilatancy constraint of neighboring material, which results in the changes of interface stresses, cannot also be considered realistically by the above classical interface models [29]. Accordingly, the mobilized interface shear strength, and the strain gradients are not calculated properly.

In the present investigation, monotonous plane shearing of an infinitely long and thin layer of a granular Cosserat material in contact with a rigid horizontal wall is analyzed. The granular material is sheared under CP and CV conditions. The analyses are conducted with FEM and an elasto-plastic Cosserat soil model. In particular, the Lade's single hardening Cosserat model is used to describe the mechanical properties of rate-independent cohesionless soil. The interaction between the granular medium and the neighboring wall is taken into account by sliding and rotating resistances of the boundary particles at the moving wall surface. The main emphasis is given to the combined effects of normal confining constraint, wall roughness, pressure level and initial void ratio on the variation of mobilized shear resistance as well as the characteristics of the localized shear zone along the wall. The obtained results of CV interface shearing are a basis to be compared with those of CP at the micro-scale level, and their differences and similarities are highlighted and discussed in the paper. The particle abrasion and crushing are not considered in the simulations conducted in the present study. This assumption can be physically and intuitively correct for stiff to very stiff particles under low to moderate stress levels (e.g., $p_0 \leq 1.0\,\mathrm{MPa}$).

Complementary DEM-based simulations are also conducted in the present study to verify the Cosserat FE results. The qualitative verification is represented in terms of distribution and evolution of field variables and state quantities within the particulate medium. Accordingly, the microscopic and macroscopic responses of the granular body under shearing are given.

The article is organized as follows: Section 1: presenting introduction; Section 2: reviewing constitutive formulations and governing equations; Section 3: giving information about FE modeling procedure, mesh discretization, and em-

ployed boundary constraints; Section 4: showing FE and DEM results and the relevant discussions; Section 5: offering conclusions.

2. Description of constitutive relations

The Cosserat theory preserves the well-posedness of the FE solutions in the post-bifurcation phase and provides mesh-independent results. The Cosserat continuum can detect the localized shear zones in the softening regime by maintaining the ellipticity of partial differential equations. So far, several Cosserat continuum models have been developed within the frame of elasto-plasticity [16, 30–37] and hypoplasticity [1, 16, 38–43] to study the interface behavior of granular materials when shear localization appears. However, some of the developed elasto-plastic Cosserat models have employed the stress limit conditions such as Von Mises, Drucker–Prager, and Mohr-Coulomb plasticity laws, which are not adequately capable to describe the real behavior of granular materials observed in experiments [30–34]. Regarding the above limitation, a more advanced elasto-plastic Cosserat constitutive model, which best fits the actual mechanical behavior of granular materials, should be used to accurately obtain the interface shear response of the granular body in touch with a bounding wall under motion.

For this purpose, the classical Lade's model given for cohesionless granular soils [44–47] is enriched to incorporate the micro-mechanical parameters including micro-rotation and couple stress through the Cosserat theory [35–37, 48, 49]. Herein, only an overview of Lade's constitutive relations along with Cosserat couple stresses and rotations is provided to make this article self-contained. Complementary information can be obtained from [35–37, 48, 49].

The elastic soil response is determined based on Hook's law [44]. The elastic modulus, E, is expressed by the conservation of energy. It varies non-linearly with the stress invariants as

$$E = MP_a[(I_I/P_a)^2 + (6(1+\upsilon)/(1-2\upsilon))(J_2'/P_a^2)]^{\lambda}, \tag{2.1}$$

where υ is the constant Poisson's ratio; I_I is the first invariant of stress tensor; J_2' is the second invariant of deviatoric stress tensor; and P_a is the atmospheric pressure with similar units as in E, I_I and J_2'. The dimensionless elastic constants (M, λ, and υ) are defined from the unloading-reloading paths of triaxial compression experiments [44].

The failure criterion is described in principal stress space by the first and the third invariants of the Cauchy stress tensor as

$$f_n = (I_I^3/I_{III} - 27)(I_I/P_a)^m, \tag{2.2}$$

where f_n is equal to η_1 at failure. This means that the present stress condition meets the peak state. The constants η_1 and m are dimensionless model parame-

ters that may be defined from the magnitudes of the deviatoric stress at failure in triaxial shear experiments. In the theory of plasticity, the plastic strain increment is given through the flow rule as $\dot{\varepsilon}_{ij}^{P} = \dot{\lambda}_p \partial g_p / \partial \sigma_{ij}$, in which $\dot{\lambda}_p$ is a positive proportionality factor; σ_{ij} is the stress tensor, and g_p is the plastic potential function, developed based on experimental data [45], and given by

$$g_p = (\psi_1 I_I^3 / I_{III} - I_I^2 / I_{II} + \psi_2)(I_I / P_a)^{\mu}, \tag{2.3}$$

where I_{II} and I_{III} are the second and third invariants of the stress tensor, respectively; ψ_2 and μ are the model constants that are specified from triaxial experiment results [47]; ψ_1 $(= 0.00155 m^{-1.27})$ is a constant associated with the curvature of the failure surface, m, as proposed in [45].

The yield criterion depends on the stress as well as the plastic work and can be expressed as

$$f_P(\sigma_{ij}, W_P) = f'_P(I_I, I_{II}, I_{III}) - f''_P(W_P) = 0, \tag{2.4}$$

where

$$f'_P = (\psi_1 I_I^3 / I_{III} - I_I^2 / I_{II})(I_I / P_a)^h e^q. \tag{2.5}$$

The parameter h is specified when the plastic work is constant along a yield surface. The constant q changes with the pressure S by $q = \alpha S / (1 - (1 - \alpha) S)$ in which α is a parameter that can be defined by the best fitting of q with the results of triaxial shear experiments [45]. The pressure amount, S, changes from zero at hydrostatic stress to unity at failure (i.e., $f_n = \eta_1$) and is determined by $S = f_n / \eta_1 = 1/\eta_1 (I_I^3 / I_{III} - 27)(I_I / P_a)^m$.

Hardening takes place when the yield function is isotropically enlarged, and the plastic work grows by

$$f''_P = (1/D)^{(1/\rho)} (W_P / P_a)^{(1/\rho)}, \tag{2.6}$$

where $\rho = P/h$ and $D = C/(27\psi_1 + 3)^{\rho}$ are material parameters. The parameters C and P can be estimated by the best fitting of Eq. (2.7) with the results of isotropic compression tests:

$$W_P = C P_a (I_I / P_a)^P. \tag{2.7}$$

In the softening regime, the yield function shrinks isotropically via

$$f''_P = A e^{-B(W_P / P_a)}. \tag{2.8}$$

The constants

$$A = (f''_P e^{(B W_P / P_a)})_{S=1} \quad \text{and} \quad B = (b(df''_P / d(W_P / P_a))(1/f''_P))_{S=1}$$

are determined from the magnitude of f''_P and the slope of the hardening curve at the peak point where $S = 1$. The constant b changes from zero to unity ($0 \leq b \leq 1.0$). The material has a perfectly plastic behavior when $b = 0$.

The Green or the Lagrangian strain tensor, E_{ij}, for the classical continuum is separated into linear and non-linear parts as

$$E_{ij} = e_{ij} + \eta_{ij} = (u_{i,j} + u_{j,i})/2 + (u_{k,i}u_{k,j})/2. \tag{2.9}$$

The quantity $u_{i,j}$ is defined as the displacement field derivative concerning the current position. The Cosserat continuum consists of particles that can deform in translation and rotation depending on the interaction between an individual particle and its neighbors. The spin or the rotation of particle is determined by ω_i^c which shows the Cosserat or material point rotation [50]. The objective or Cosserat strain rate tensor is defined by

$$\dot{\gamma}_{ij} = \dot{E}_{ij} + (\dot{\Omega}_{ij} - \dot{\Omega}_{ij}^c). \tag{2.10}$$

Equation (2.10) represents two types of spin tensors [51], which are the classical and Cosserat spins and determined by

$$\dot{\Omega}_{ij} = 1/2(\nu_{i,j} - \nu_{j,i}), \tag{2.11}$$

$$\Omega_{ij}^c = -e_{ijk}\omega_k^c, \tag{2.12}$$

where e_{ijk} is the Ricci permutation symbol. The classical spin represents the rigid body rotation or environmental rotation of a material element resulting from the macro-motion. Generally, the Cosserat strain rate tensor, given in Eq. (2.10), generates asymmetry in the stress tensor [52]. In the particular case, when the Cosserat rotation is the same as the environmental rotation, the symmetric strain rate tensor for the classical continuum will be obtained. The micro-curvature vector of deformation or the gradient of Cosserat rotation is described by

$$\kappa_{ij} = \omega_{j,i}^c. \tag{2.13}$$

In the Cosserat continuum, static quantities are the Cauchy stress tensor, σ_{ij}, and the couple stress tensor, M, which are determined concerning the current configuration of a continuum body. Considering the effects of couple stresses, the equilibrium equations in the Cosserat continuum are expressed by

$$\sigma_{ij,j} + b_i = 0, \tag{2.14}$$

$$M_{ij,j} - \epsilon_{ijk}\sigma_{jk} + c_i = 0, \tag{2.15}$$

where b and c are the body force and the body couple per unit volume, respectively. Routinely, c is neglected in granular bodies. In general, the stress tensor

is asymmetric in the Cosserat continuum due to the presence of couple stresses (i.e., $\epsilon_{ijk}\sigma_{jk} \neq 0$), except for the conditions where $M_{ij,j} = 0$ and $c_i = 0$ [41, 48].

The equilibrium condition for a Cosserat body with volume V is written in the weak form as

$$\int_V [\delta\dot{u}_i\sigma_{ij,j} + \delta\dot{u}_i\rho b_i + \delta\dot{\omega}^c_k M_{kj,j} - \delta\dot{\omega}^c_k\epsilon_{kij}\sigma_{ij} + \delta\dot{\omega}^c_k\rho c_k]\, dV = 0, \tag{2.16}$$

where ρ denotes the spatial mass density. The velocity components, $\dot{u}_i$, and the Cosserat angular velocity, $\dot{\omega}^c_k$, are independent of the static quantities. By applying Gaussian integration, the following equation can be obtained:

$$\int_V [\delta\dot{u}_i\,\rho\, b_i + \delta\dot{\omega}^c_k\,\rho\, c_k]\, dV + \int_S [\delta\dot{u}_i\,\sigma_{ij}\,n_j + \delta\dot{\omega}^c_k\, M_{kj}\, n_j]\, dS - \int_V [\delta\dot{\omega}^c_k\epsilon_{kij}\sigma_{ij} + (\delta\dot{u}_i)_{,j}\sigma_{ij} + (\delta\dot{\omega}^c_k)_{,j}M_{kj}]\, dV = 0, \tag{2.17}$$

where $t_i = \sigma_{ij}n_j$ is the surface traction; $m_k = M_{kj}n_j$ is the surface couple; and n_j is the outward normal unit vector prescribed on the boundary surface, S. With Eq. (2.17), the boundary conditions can better be understood. Besides the stress and displacement boundary constraints of a conventional continuum (t_i or u_i), extra non-standard Cosserat kinematical boundary constraints, i.e. micro-rotation or surface couple (m_k or $\dot{\omega}^c_k$) must be prescribed on the boundaries of a Cosserat continuum body.

Lade's model has been developed based on the stress invariants and it needs all three invariants to update all field quantities. The second invariants of stress and deviatoric stress tensors are rewritten in the Cosserat continuum to incorporate the couple stress effects as

$$I_{II} = h_1(\sigma_{12}\sigma_{21} - \sigma_{11}\sigma_{22} - \sigma_{11}\sigma_{33} - \sigma_{22}\sigma_{33}) - h_2 m_1 m_2/l^2, \tag{2.18}$$

$$J_2' = h_3\{[(\sigma_{11} - \sigma_{22})^2 + (\sigma_{33} - \sigma_{22})^2 + (\sigma_{11} - \sigma_{33})^2] + ((\sigma_{12} + \sigma_{21})/2)^2\} + h_4(m_1^2 + m_2^2)/l^2, \tag{2.19}$$

where m_i are the couple stress components ($m_1 = M_{31}$, $m_2 = M_{32}$); and l (= the mean particle size, d_{50}) is the intrinsic length scale. Vardoulakis and Sulem (1995) applied the same technique to adjust the stress invariants [33].

In the plane strain Cosserat continuum, the stress and strain tensors are given in the following vector forms as

$$\{\sigma\} = \{\sigma_{11}\ \ \sigma_{22}\ \ \sigma_{33}\ \ \sigma_{12}\ \ \sigma_{21}\ \ m_1/l\ \ m_2/l\}^T, \tag{2.20}$$

$$\{\gamma\} = \{\gamma_{11}\ \ \gamma_{22}\ \ \gamma_{33}\ \ \gamma_{12}\ \ \gamma_{21}\ \ l\kappa_1\ \ l\kappa_2\}^T, \tag{2.21}$$

where κ_i are the micro-curvature components ($\kappa_1 = \kappa_{31}$, $\kappa_2 = \kappa_{32}$). It is preferred to use time rates for stress and strain as

$$\{\dot{\sigma}\} = [D]\{\dot{\gamma}\}, \tag{2.22}$$

where $[D]$ is the elasto-plastic stiffness matrix developed in the Cosserat continuum [35, 48].

The classical Lade's model involves 11 constants that can be specified by one isotropic compression test with unloading-reloading paths and three triaxial shear tests [35, 45–48]. The constants are related to non-linear elasticity (M_L, λ and υ), material hardening and softening (C and P), failure criterion (η_1, m), yield function (α, h), and plastic potential function (ψ_2 and μ). These constants are determined analogously in both Cosserat, and classical versions of the model [45–47] as the Cosserat effects are not initiated in co-axial and homogeneous deformations with zero couple stresses. However, the Lade's Cosserat model has five additional constants, including the four weighing factors (h_1 to h_4) which are employed to enrich the stress invariants presented in Eqs. (2.18) and (2.19) and the average particle size ($d_{50} = 1$ mm). The model properly relates the intrinsic length scale to d_{50} [33, 58, 59], which is predicted from the particle size distribution. The weighing parameters (h_1 to h_4) are determined based on the contact distribution of particles [35, 53, 54]. These parameters are assumed to be equal to one in the current study, as recommended by [33]. The calibration procedure of the model constants is briefly explained in the following, and the details have been presented in [35, 45–48].

Non-linear elasticity constants (M_L, λ *and* υ): these constants generate elastic strains due to the variation of stresses. According to Hooke's law, the non-linear elastic modulus, E, can be determined via the unloading-reloading paths in triaxial shear experiment. Poisson's ratio is computed using the primary slope of the volume change curve through $\upsilon = -(\Delta\varepsilon_3/\Delta\varepsilon_1) = (1 - (\Delta\varepsilon_v/\Delta\varepsilon_1))/2$. Whenever the Poisson's ratio was determined, Eq. (2.1) is rewritten to calculate M_L and λ via $\log(E/P_a) = \log M_L + \lambda \log[(I_I/P_a)^2 + (6(1+\upsilon)/(1-2\upsilon))(J_2'/P_a^2)]$. To this end, $[(I_I/P_a)^2 + (6(1+\upsilon)/(1-2\upsilon))J_2'/P_a^2]$ is plotted against (E/P_a) on a log-log scale. The intersection of the best-fitting line passing through the laboratory results with a vertical axis of $\log[(I_I/P_a)^2 + (6(1+\upsilon)/(1-2\upsilon))J_2'/P_a^2] = 1$ is equal to M_L, and the slope of this line is equal to λ. As a minimum, three triaxial shear experiments with varied confining stresses are needed to properly draw the best-fitting line.

Material hardening and softening constants (C *and* P): in order to predict these constants, (W_P/P_a) is plotted against (I_I/P_a) on a log-log scale. C is defined by the intersection of the best-fitting line passing through the laboratory results with a vertical axis of $\log(I_I/P_a) = 1$, and P is the slope of this line.

Failure criterion constants (η_1, m): the failure criterion can be rewritten as $\log((I_I^3/I_{III}) - 27) = \log \eta_1 + m(P_a/I_I)$. Then, (P_a/I_I) is plotted against $((I_I^3/I_{III}) - 27)$ at failure on a log-log scale. The intersection of the best-fitting line passing through the laboratory results with a vertical axis of $\log(P_a/I_I) = 1$, is η_1, and the slope of this line is equal to m.

Yield function constants (α, h): the plastic work is unique along the yield surface, and subsequently, the driving stress is also unique. If two stress paths are taken into account, OA along the hydrostatic axis, and OB along an arbitrary stress path on the failure surface, then $f'_{PA} = f'_{PB}$ occurs, and h is determined by

$$h = (\ln((\psi_1(I_{IB}^3/I_{III\,B}) - (I_{I\,B}^2/I_{II\,B}))e/(27\psi_1 + 2))/\ln(I_{I\,A}/I_{I\,B}))$$

in which e is the base of the natural logarithm. All the above predicted constants are then used to determine the stress level parameter:

$$q = \ln(((W_P/(DP_a))^{1/\rho})/((\psi_1(I_I^3/I_{III}) - (I_I^2/I_{II}))(I_I/P)^h))).$$

Subsequently, the experimental data set is applied to plot S against q to obtain α.

Plastic potential function constants (ψ_2 *and* μ): in order to define these constants,

$$\xi_x = (1/(1+\upsilon))((I_I^3/I_{II}^2)(\sigma_1 + \sigma_3 + 2\upsilon\sigma_3) + \psi_1(I_I^4/I_{III}^2)(\sigma_1\sigma_3 + \upsilon\sigma_3^2)) - 3\psi_1(I_I^3/I_{III}) + 2(I_I^2/I_{II})$$

and

$$\xi_y = \psi_1(I_I^3/I_{III}) - (I_I^2/I_{II})$$

are calculated at failure for a particular experimental data set; afterward ξ_y is plotted against ξ_x on an arithmetic scale. The data set can be best fitted by a line with the slope of $1/\mu$. The intersection of this line with the vertical axis is $-\psi_2$. As a minimum, three triaxial shear experiments with varying confining stresses are needed to properly draw the line.

The constitutive constants used in the numerical simulations of the present study are those measured for a medium dense fine silica sand [35, 48] and shown in Table 1.

Table 1. Lade's model parameters for fine silica sand.

Description	Lade's model parameters	Value
Elastic properties	M_L, λ, υ	292.6, 0.25, 0.13
Failure criterion	m, η_1	0.37, 84.1
Plastic potential	μ, ψ_2	2.2, −3.06
Yield criterion	h, α	0.95, 0.3
Hardening/softening law	C, P	7e-5, 2.6, 1.0

Lade's model enhanced with Cosserat quantities has been implemented into a non-linear FE program [55]. Due to space limitations, only the essential components of the model have been presented here. The numerical implementation aspects have already been discussed in detail by [35–37, 49]. The enhanced Lade's Cosserat model has successfully been employed in simulating biaxial compression test [49, 56], reinforced soil structures [57], pull-out behavior of geogrid [58, 59], shear behavior of granular body [60–62], and interface behavior of granular medium [35–37]. In the mentioned investigations, the numerical results have been confirmed by experimental observations.

3. FE modelling of interface shearing

In the current research, the interface behavior of an infinitely long cohesionless granular soil layer sheared against a bottom wall of varying surface roughness is studied under constant normal pressure (CP) and constant volume (CV) conditions, Fig. 1(a, b). The layer is discretized by four-node Cosserat elements with a size of 1.25 mm × 1.25 mm. The element size is small enough and lower than $5 \times d_{50}$ (with $d_{50} = 1$ mm) to obtain mesh independent results [38]. To define the translational and rotational degrees of freedom in the two-dimensional (2D) element, a quadrilateral four-node isoparametric element with bi-linear shape functions and four integration points is employed [35–37, 49]. According to Fig. 1, numerical calculations are performed for a medium dense granular soil layer with b = width = 10 cm and h_0 = initial height = 4 cm. For the base case, e_0 = initial void ratio = 0.6 and p_0 = initial isotropic pressure = 100 kPa are assumed.

Regarding the interaction process between granular medium and neighboring wall, boundary particles may trap within the asperities of the wall's surface. Hence, neither particle sliding nor particle rolling may occur along the interface. Consequently, the relative displacement and the micro-rotation at the lower surface of granular medium is negligible [35, 59–63]. However, simultaneous shear and slip of the materials occur along rough, medium rough and relatively smooth surfaces and under quasi-static processes. The absence of particle sliding and rolling adjacent to very rough walls was verified in silo model tests with coins and Couette shear tests with steel rods [1, 15, 64]. Accordingly, the below relations are derived based on an elasto-plastic Cosserat continuum to realistically simulate a wide range of wall asperities from rough to smooth conditions (Fig. 1):

(i) Boundary particles of the granular medium are in permanent contact with the neighboring wall. Therefore, the relative displacement of boundary particles in the direction normal to the wall surface, u_{2r}, is zero, i.e.:

$$u_{2r} = U_{2B} - u_{2p} = 0. \tag{3.1}$$

(ii) The tangential displacement of the first layer of boundary particles in the direction of shear movement, u_{1P}, is equal to or less than the displacement of wall boundary, U_{1B}, i.e.:

$$u_{1p} = f_u U_{1B}. \tag{3.2}$$

The dimensionless parameter $0 \leq f_u \leq 1$ represents a portion of U_{1B} that is transferred to the boundary particles of the granular medium.

(iii) The relative displacement, u_{1r}, between the boundary surfaces of two bodies reads:

$$u_{1r} = U_{1B} - u_{1p} = (1 - f_u)U_{1B}, \tag{3.3}$$

u_{1r} can also be denoted as the sum of the fraction due to particle sliding, u_{1rs}, and the fraction due to particle rotation, u_{1rr}, i.e.:

$$u_{1rs} = f_s U_{1B}, \tag{3.4}$$

$$u_{1rr} = f_r U_{1B}, \tag{3.5}$$

$$u_{1r} = u_{1rs} + u_{1rr} = (f_s + f_r)U_{1B}. \tag{3.6}$$

Here, f_s and f_r represent the portions of U_{1B} that are transferred by sliding and rotating, respectively. A comparison between Eqs. (3.3) and (3.6) yields the following relation:

$$f_u + f_r + f_s = 1. \tag{3.7}$$

Equation (3.7) includes the following extreme conditions:

(a) No rolling: $f_r = 0$, so that $f_s = 1 - f_u$ and $u_{1r} = u_{1rs} = (1 - f_u)U_{1B}$.

(b) Neither sliding nor rolling: $f_r = f_s = 0$, so that $f_u = 1$ and no relative displacement occurs: $u_{1r} = 0$.

(c) Pure rolling: $f_s = 0$, so that $f_u + f_r = 1$.

(iv) The following relation is proposed between the micro-rotation at the boundary of granular medium, ω_p^c, the mean particle size, d_{50}, the parameter f_r, and the displacement U_{1B}, [36, 37]:

$$\omega_p^c = f_r(U_{1B}/(d_{50}/2)), \tag{3.8}$$

ω_p^c is also given by the boundary particle displacement at the bottom of the granular medium, u_{1p}, i.e.:

$$\omega_p^c = (f_r/f_u)(u_{1p}/(d_{50}/2)) \tag{3.9}$$

or by the relative displacement, u_{1r}, i.e.:

$$\omega_p^c = (f_r/(1 - f_u))(u_r/(d_{50}/2)). \tag{3.10}$$

(v) Regarding Eq. (3.10), correlation (3.11) for ω_p^c is also expressed by the particle displacement at the wall surface, u_{1P}, i.e.:

$$\omega_p^c = f_w(u_{1p}/d_{50}) \tag{3.11}$$

with $f_w = 2f_r/f_u$. The proportionality coefficient, f_w, depends on the interaction between particles at the bottom boundary of the granular medium and adjoining wall. In general, factors f_r, f_s, f_u, and f_w changes with variation of field variables in the granular medium in a more complicated manner [29, 41]. For the purpose of simplification, however, these factors are assumed to be constant in the current investigation. f_w has empirically been related to the relative roughness of the bottom wall's surface by $f_w = F(r_w/d_{50})$, in which F is the so-called interface function [15, 35, 36, 43]. The proportionality coefficient, f_w, denotes u_{1P} fraction, transmitted to particles via rotation. Thus, a lower value for f_w corresponds to smaller particle rotation at the wall's surface representing a rough surface condition. According to UESUGI *et al.* [65], the roughness of boundary can be characterized by the height of the surface asperities, r_w, measured on a representative area. Here, a relatively smoother wall corresponds to a higher f_w value and vice versa. This implies that f_w has an inverse relationship with wall roughness (r_w). Smooth walls are identified when the boundary particles are large enough relative to any surface asperities, Fig. 1(d, e). The coefficient, f_w, can be measured from the wall friction experiments taking into account the effects of wall roughness, r_w, and average particle size, d_{50}, of the granular materials [1, 15, 43, 64, 66]. Additionally, f_w and Cosserat boundary conditions can also be verified by 3D DEM simulations with non-spherical particles [67, 68].

Two special extreme cases of shearing under CP and CV confining constraints are simulated using FEM, Fig. 1(a,b). Both cases can impose infinite shearing condition on the soil-wall interface. The boundary constraints of the soil body under CP shearing are:

$$\begin{aligned} &u_1(x_1,0) = U_{1B}, \quad u_2(x_1,0) = 0, \quad \omega_3^c(x_1,0) = \omega_p^c(x_1,0) = -f_w U_{1B}/l, \\ &u_1(x_1,h) = 0, \ \sigma_{22}(x_1,h) = -p_0 = -100\,\mathrm{kPa}, \ \omega_3^c(x_1,h) = \omega_p^c(x_1,h) = 0. \end{aligned} \tag{3.12}$$

While the boundary conditions of the soil body subjected to CV shearing are:

$$\begin{aligned} &u_1(x_1,0) = U_{1B}, \quad u_2(x_1,0) = 0, \quad \omega_3^c(x_1,0) = \omega_p^c(x_1,0) = -f_w U_{1B}/l, \\ &u_1(x_1,h) = 0, \quad u_2(x_1,h) = 0, \quad \omega_3^c(x_1,h) = \omega_p^c(x_1,h) = 0. \end{aligned} \tag{3.13}$$

Herein, h represents the thickness of soil layer; $h \gg d_{50}$ is taken into account and, consequently, the upper boundary of the layer has a negligible effect on

developing the wall shear zone. In the considered normal boundary conditions, Cosserat rotations are constrained at the upper boundary of the layer, while a specific coupling is prescribed between the shear movement of the bounding wall and the corresponding Cosserat or micro-rotation at the lower boundary of the layer. Here, a very rough surface condition has been assumed along the upper boundary of the granular layer via locked Cosserat rotations [35, 40, 41, 63]. However, a proportional kinematic relation between the applied shear displacement and the corresponding Cosserat rotation at the top boundary, can also be taken into account to describe rough, medium rough, or relatively smooth surfaces, as in [36]. In fact, the assumption of locked Cosserat rotations along the top surface of the layer indicates only a special distribution of shear stresses and void ratios close to this area. Other kinds of distributions can also be considered at the upper boundary by introducing different roughness conditions via various degrees of constraints of Cosserat rotations.

In CP condition, the upper boundary of the layer ($x_2 = h$) is only restricted in the horizontal orientation not to happen sliding and rotating, while the layer is free in the vertical direction. Thus, the vertical displacement is produced due to the dilatancy or contractancy of the entire layer, and a normal stress (p_0) is constantly imposed on the upper boundary. Therefore, the layer height is not fixed and can vary in the course of shearing. While in CV condition, the upper boundary of soil layer ($x_2 = h$) is restricted in both horizontal and vertical orientations. Along the lower surface of the layer ($x_2 = 0$), the vertical movement (u_2) is restricted in both CP and CV conditions, and the applied shear movement is equal for the bottom wall (U_{1B}) and the lower boundary of the soil layer (u_{1B}). This means that the relative shear movement along the interface, caused by the lower skin frictions, is not taken into account [69, 70]. The wall movement, U_{1B}, is transferred to the soil body by the surface roughness. A large shear movement is initiated by moving the bottom surface nodes of the soil layer horizontally ($U_{1B} = u_{1B}$). Since the behavior assumed for the granular soil is rate-independent, the considered time step can be related, for example, to the displacement increment. The numerical simulations are carried out in an updated Lagrange frame, which is efficient for dealing with large deformations and strain localization in the material.

In a Cartesian reference system and for 2D condition, the kinematic variables are displacements (u_1 and u_2) and micro-rotation (the Cosserat rotation, ω_3^c), and the non-zero static variables are stress components (σ_{11}, σ_{22}, σ_{33}, σ_{12}, σ_{21}) and couple stress components (m_1, m_2), Fig. 1(c).

For simulation of an infinitely long and thin granular layer, the discretization of a limited profile with finite elements is only needed, assuming the primary condition of the soil medium is uniform [39]. The symmetry condition of the infinite granular layer is provided by imposing appropriate restrictions to the

lateral boundaries of the layer, i.e., each node on the left boundary is constrained to the corresponding node on the right boundary to have similar displacements and micro-rotation. So that the numerical results do not depend on the horizontal coordinate and the length of the FE mesh [39]. Consequently, $\gamma_{11}=\gamma_{33}=\kappa_{31}=0$, and the non-zero components of objective strain rate and micro-curvature rate tensors are:

$$\begin{aligned} &\dot{\gamma}_{22}=\partial\dot{u}_2/\partial x_2, \quad \dot{\gamma}_{12}=\partial\dot{u}_1/\partial x_2+\dot{\omega}_3^c=\dot{\omega}_3^c-2\dot{\omega}_3,\\ &\dot{\gamma}_{21}=-\dot{\omega}_3^c, \quad \dot{\kappa}_{32}=\partial\dot{\omega}_3^c/\partial x_2. \end{aligned} \tag{3.14}$$

Herein, $\dot{\omega}_3=-(\partial\dot{u}_1/\partial x_2)/2$ represents the environmental angular velocity from macro-motion. Due to the lack of body force, body couple and inertia forces, the equilibrium equations in the plane strain condition for the infinite shear layer yield:

$$\partial\sigma_{12}/\partial x_2=0, \quad \partial\sigma_{22}/\partial x_2=0, \quad \partial M_{32}/\partial x_2-(\sigma_{12}-\sigma_{21})=0. \tag{3.15}$$

The rate forms of equilibrium equations then read:

$$\partial\dot{\sigma}_{12}/\partial x_2=0,\ \partial\dot{\sigma}_{22}/\partial x_2=0,\ \partial\dot{M}_{32}/\partial x_2-D_{22}^R(\sigma_{12}-\sigma_{21})-(\dot{\sigma}_{12}-\dot{\sigma}_{21})=0. \tag{3.16}$$

This means that the stress components σ_{12} and σ_{22} are constant across the granular layer height; and the difference of two shear stress components is relevant to the gradient of couple stress on horizontal planes. Accordingly, D_{22}^R is the relative deformation rate tensor.

The infinite shear layer is modeled as an elasto-plastic Cosserat material and considered to be homogeneous and isotropic at the initial state, i.e.:

$$(\sigma_{ij})_{t=0}=-p_0\delta_{ij}, \quad (m_i)_{t=0}=0, \quad (e)_{t=0}=e_0. \tag{3.17}$$

The above assumptions show that the shear and couple stresses are zero at the initial state, i.e., $\sigma_{12}=\sigma_{21}=M_{31}=M_{32}=0$. Hence, the time derivative of shear and couple stresses coincide with their objective rates at the initial state:

$$\dot{\sigma}_{12}=\overset{\circ}{\sigma}_{12}, \quad \dot{\sigma}_{21}=\overset{\circ}{\sigma}_{21}, \quad \dot{M}_{31}=\overset{\circ}{M}_{31}, \quad \dot{M}_{32}=\overset{\circ}{M}_{32}. \tag{3.18}$$

In Section 4.1, the coupled influences of the normal confining condition and the bounding wall roughness are examined on the shear response of a granular Cosserat layer. Special emphasis is given to the development of strain localization in the material. In addition, a parametric study is performed in Section 4.2 to evaluate the influences of pressure level (p_0 = 100, 500, 1000 kPa) and initial void ratio (e_0 = 0.60, 0.75, 0.90) on the interface response of the shear

layer. In Section 4.3, complementary DEM-based simulations of interface shearing are conducted to qualitatively verify the results of Cosserat FE analyses. It is noteworthy that the lateral boundary conditions in DEM simulations of the interface shear test are different from those of FE analyses of the infinite shear layer. Consequently, DEM results are obtained at the mid-section of the granular specimen far from the sidewalls to minimize the lateral boundary effects. In addition, for comparison purposes, particle crushing phenomenon is not taken into account in DEM simulations similar to FE analyses. However, this phenomenon will be dominant at higher pressure levels, and particularly in shearing under CV condition.

4. Numerical results of interface shearing

4.1. The influences of normal confining constraint and wall roughness

The results of interface behavior of an initially homogeneous and isotropic granular layer ($e_0 = 0.6$) sheared under CP and CV normal confining conditions are explained in relation to Figs. 2–11. In simulations, the surface roughness magnitudes of the bottom wall are set as $f_w = 0.05$, 0.10, 0.25, 0.50 representing rough ($f_w = 0.05$), medium rough ($f_w = 0.10$, 0.25) and relatively smooth ($f_w = 0.5$) conditions. All figures are displayed for different values of normalized shear movement of the bounding wall ($U_{1B}/h_0 = 0.25$, 1.00 and 2.00).

During different stages of wall movement, shear displacement, u_1, gradually develops within the soil layer under both normal boundary conditions, as plotted in Figs. 2(a) and 3(a). According to the figures, further increase of wall displacement, U_{1B}, causes localization of shear deformations along the bottom wall's surface. It is revealed that the development of shear deformations outside the wall shear zone is more pronounced in CV condition compared to that of CP condition. Although the additional horizontal displacements outside the localized shear zone are nearly zero in the rough interfaces under CP condition (Fig. 2(aA, aB)), they are continuously developed in those of CV condition (Fig. 3(aA, aB)).

For relatively smooth walls, e.g., $f_w = 0.5$ displayed in Figs. 2(aD) and 3(aD), minor deformation occurs within the granular medium. Accordingly, only the soil particles adjacent to the interface are expected to contribute to the soil-wall interaction, and the involvement of upper parts farther away from the interface is negligible. In this regard, particle movements are limited to a narrow zone near the bounding wall with a thickness of around one particle size, and they lessen quickly with rising distance from the wall, Figs. 2(aD) and 3(aD). Particularly, they are around zero in areas that are far away from the moving wall. Nevertheless, if the wall roughness increases, e.g., $f_w = 0.05$, as shown in Figs. 2(aA) and 3(aA), more soil particles in the granular layer, and not only those close to

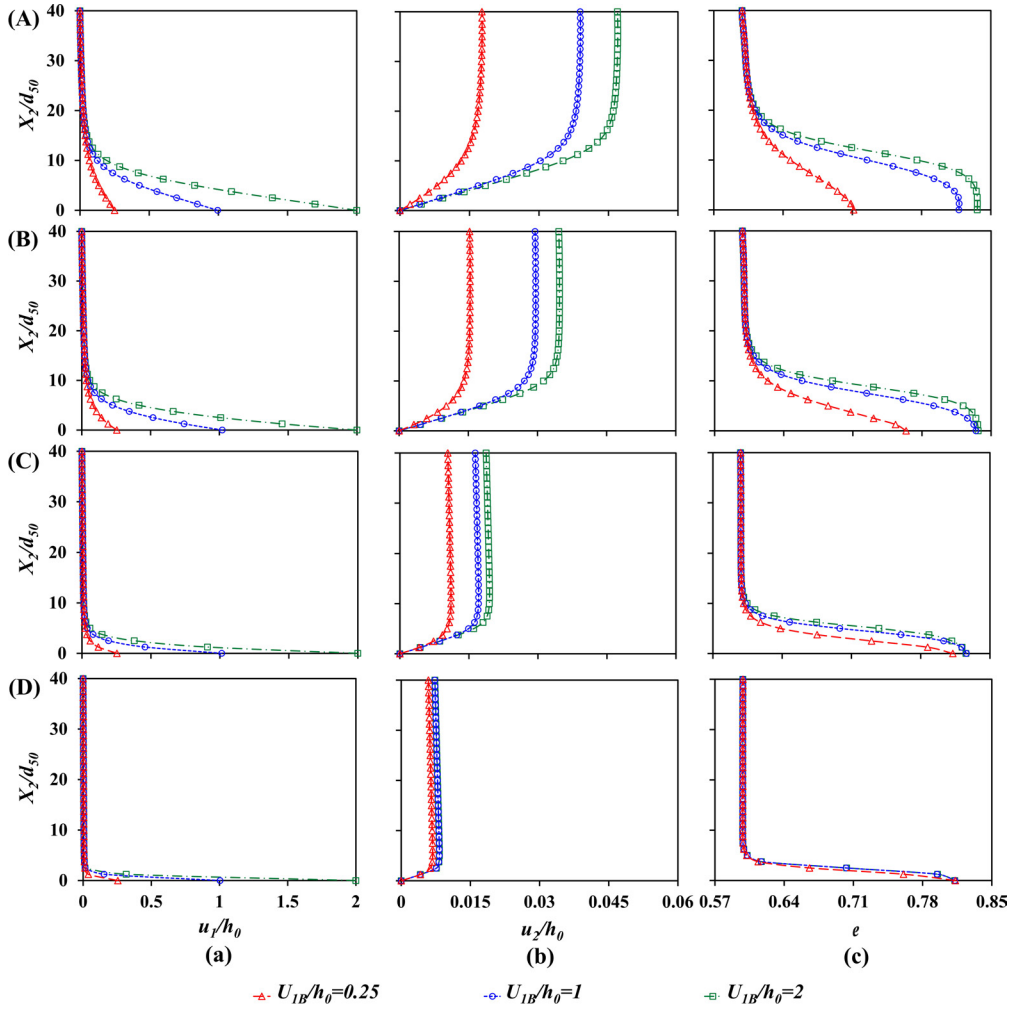

FIG. 2. Variation of (a) u_1/h_0, (b) u_2/h_0 and (c) e across X_2/d_{50} at different U_{1B}/h_0 in CP shearing for: (A) *Case* (1): $f = 0.05$, (B) *Case* (2): $f = 0.10$, (C) *Case* (3): $f = 0.25$ and (D) *Case* (4): $f = 0.5$.

the wall, may be involved in the shearing process. In fact, a rough wall contains many asperity valleys at the size of particle, which may trap boundary particles, Figs. 2(aA) and 3(aA). This trapping effect cannot be achieved in smooth surfaces, and the wall movement can hardly be transferred to the granular layer, Figs. 2(aD) and 3(aD). Hence, a very thin area near the wall is only affected by shearing, developing a narrow wall shear zone.

Concerning Figs. 2(b) and 3(b), the vertical deformation, u_2, varies nonlinearly across the layer height. The vertical deformation is related to the dilation

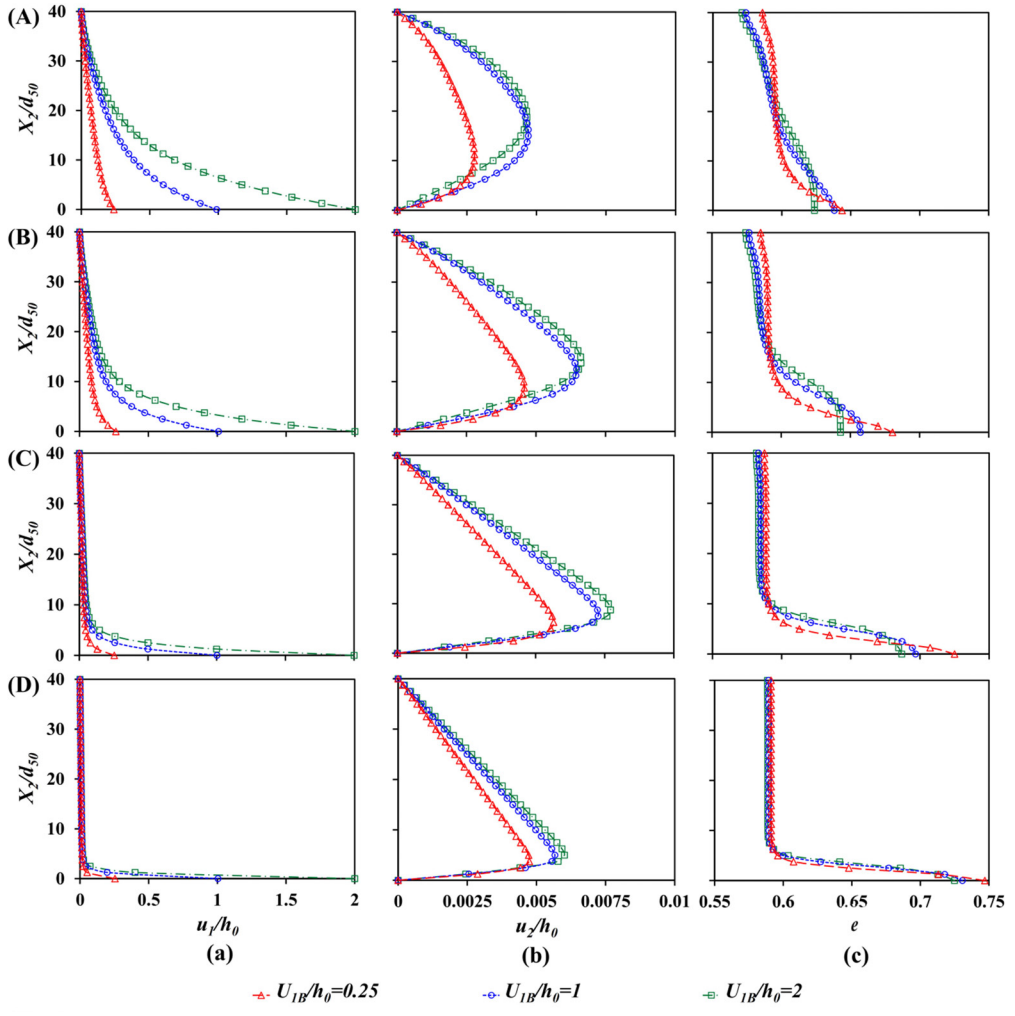

Fig. 3. Variation of (a) u_1/h_0, (b) u_2/h_0 and (c) e across X_2/d_{50} at different U_{1B}/h_0 in CV shearing for: (A) *Case* (1): $f = 0.05$, (B) *Case* (2): $f = 0.10$, (C) *Case* (3): $f = 0.25$ and (D) *Case* (4): $f = 0.5$.

of the thin zone of material being involved in the shearing process. The layer height changes when it is sheared under the CP condition, as also presented in Fig. 2(b). It is also seen in the figure that the soil volume expands as long as the normalized shear movement of the adjacent wall becomes larger. The vertical deformation profile above the wall shear zone in CP condition, which is reflecting the progressive soil dilation, possesses no deformation gradient that reveals the granular layer is uniformly traveling away from the wall. On the contrary, the height of the shear layer is constant during CV shearing, Fig. 3(b).

The lower boundary of the granular medium hinders vertical displacement in both confining conditions because of the existence of a rigid wall. In the case of negligible soil volume change in relatively smooth walls under CV condition, e.g., $f_w = 0.5$, dilation happens directly next to the wall and is proportionally compensated by the contraction of the neighboring soil, Fig. 3(bD). As depicted in Figs. 2(a, b) and 3(a, b), the shear deformations are inhomogeneous within the granular Cosserat layer under both normal confining constraints from the start of shearing.

The wall shear zone can be identified by a substantial increase of void ratio (e). The distribution patterns of void ratio across the layer height are entirely different for various wall roughness values, Figs. 2(c) and 3(c). For shearing under CP, the soil volume enlarges due to substantial dilation in the wall shear zone, Fig. 2(b, c). However, dilation in the shear zone causes compression in the rest part of the granular body for shearing under CV, Fig. 3(b, c). Thus, the requirement for constant volume is globally fulfilled, i.e., the integral of the void ratio curve across the layer height remains constant. Dilation in the shear zone accompanied by contraction in the other parts of the shear layer can be observed from the distribution of void ratio, whereas the mean value of the void ratio keeps constant, Fig. 3(c). The void ratio profile is non-linear across the layer height, Figs. 2(c) and 3(c). Thus, an originally uniformly distributed void ratio in the granular layer becomes heterogeneous in the course of shearing due to localization, as already studied with more details, for example, in [41]. The void ratio value does not nearly depend on the coordinate X_2, except for the limited zones near the top and bottom boundaries of the shear layer. The deviation near the top is due to the Cosserat boundary constraints prescribed at the upper boundary of the soil medium.

It is seen in Figs. 4(a) and 5(a) that the Cosserat or micro-rotation (ω_3^c) is nearly constant across the layer height with the exception of the lower parts close to the bottom surface. Significant particle rotations with dilatancy are seen in the granular medium adjacent to the bottom wall with continuing displacement in both CP and CV shearing, Figs. 2(c), 3(c), 4(a) and 5(a). They arise spontaneously from the beginning of shearing.

Variation and magnitude of normalized couple stress, m_2^*, depend significantly on the normal confining constraint and wall roughness, Figs. 4(b) and 5(b); m_2^* is non-uniformly distributed across the layer height. Regardless of the shear displacement amount, the couple stress is zero in the middle of the wall shear zone. It can be pointed out that the normalized couple stress, m_2^*, is minimal in CP condition (Fig. 4(b)), but it does not disappear in the granular medium. According to Eq. (3.15), the normalized couple stress, m_2^*, indicates the extrema in the positions at which the normalized shear stresses, σ_{12}^* and σ_{21}^*, are the same, Figs. 6(b, c) and 7(b, c). The gradient of normalized couple stress, m_2^*,

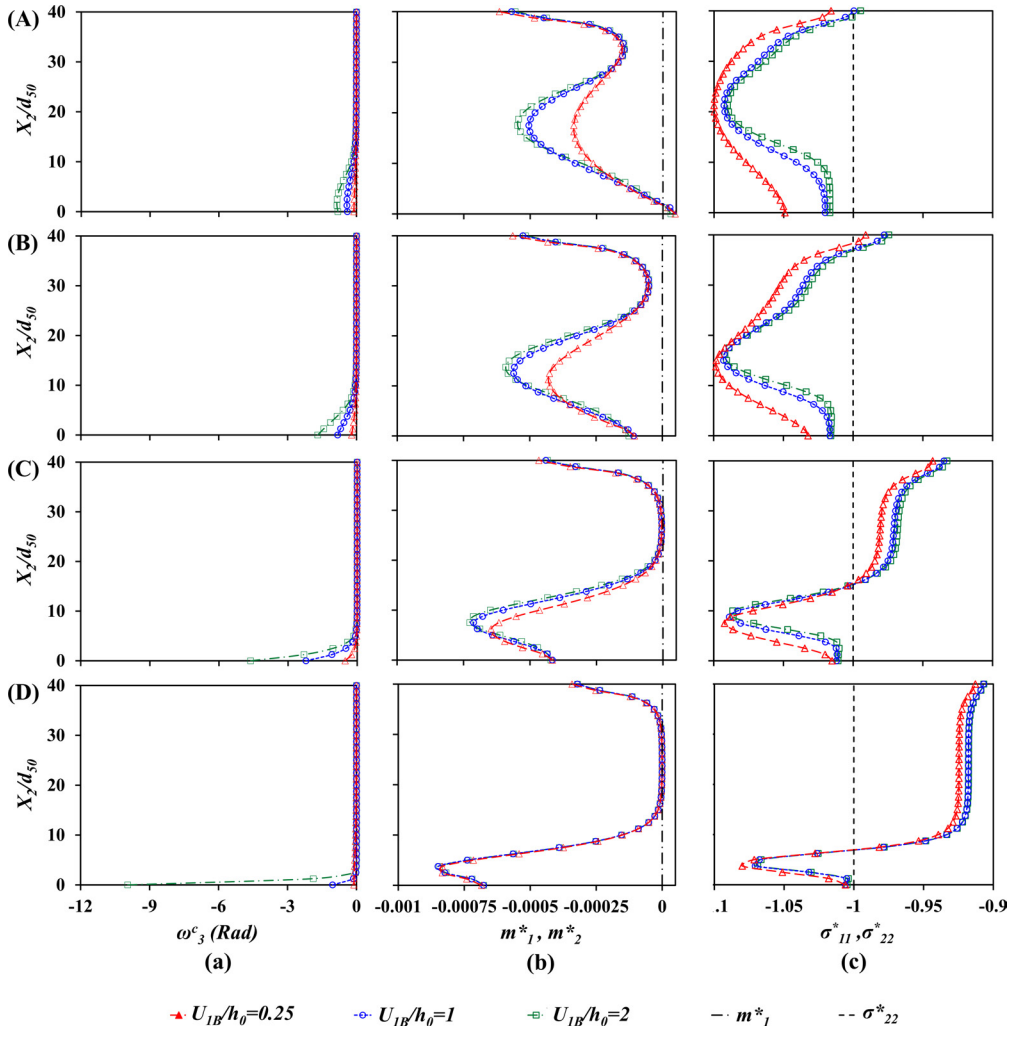

FIG. 4. Variation of (a) ω_3^c, (b) $m_{1,2}^*$ and (c) σ_{11}^*, σ_{22}^* across X_2/d_{50} at different U_{1B}/h_0 in CP shearing for: (A) *Case* (1): $f = 0.05$, (B) *Case* (2): $f = 0.10$, (C) *Case* (3): $f = 0.25$ and (D) *Case* (4): $f = 0.5$.

is relevant to the difference of normalized shear stresses, $(\sigma_{12}^* - \sigma_{21}^*)$. In spite of the fact that no localization is identified close to the upper surface, normalized couple stresses jump dramatically in this region, and the stress tensor is asymmetric, Figs. 4(b) and 5(b). As previously explained, this difference is related to the Cosserat constraints prescribed at the upper boundary of the soil medium.

Based on Figs. 6(a, b) and 7(a, b), uniform distribution of stress components σ_{12}^* and σ_{22}^* are obtained as required for equilibrium given in Eqs. (2.15, 3.15,

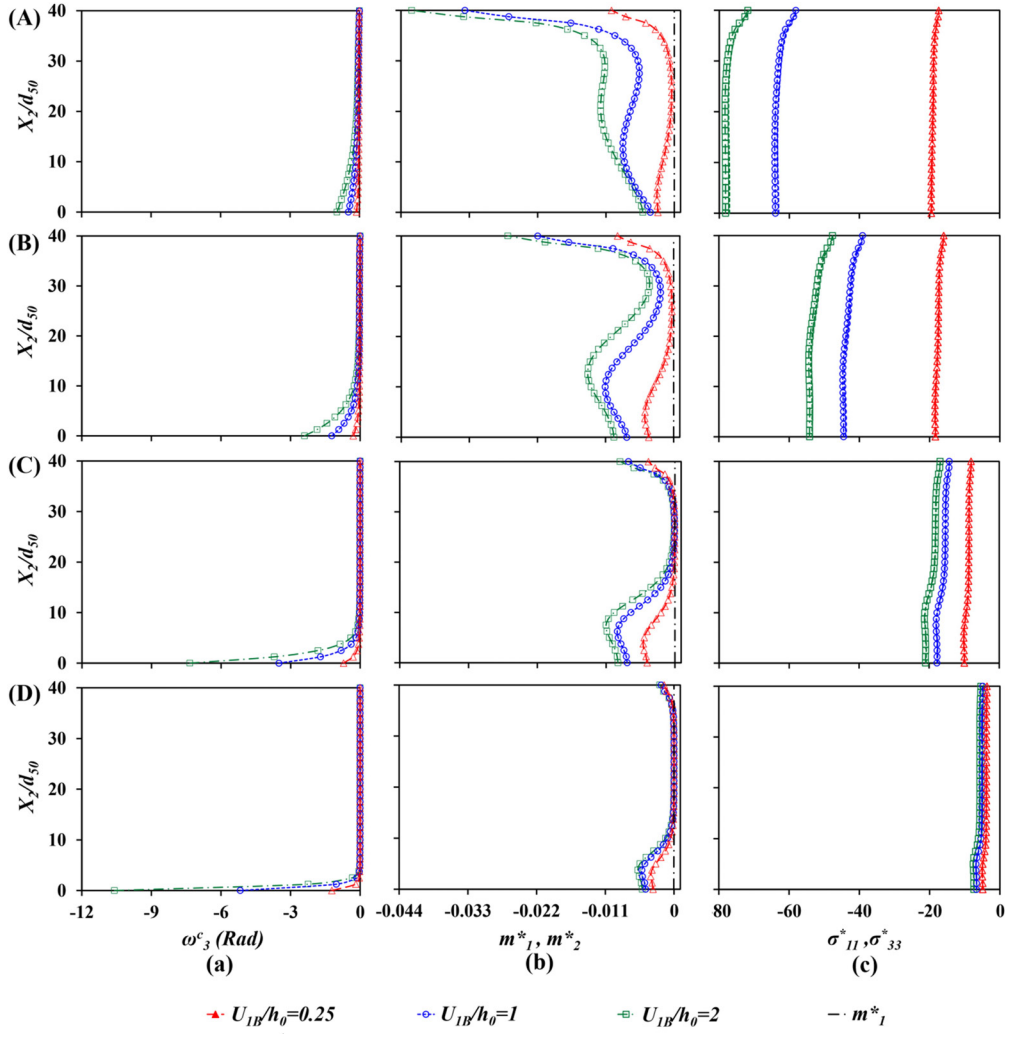

FIG. 5. Variation of (a) ω^c_3, (b) $m^*_{1,2}$ and (c) σ^*_{11}, σ^*_{33} across X_2/d_{50} at different U_{1B}/h_0 in CV shearing for: (A) *Case* (1): $f = 0.05$, (B) *Case* (2): $f = 0.10$, (C) *Case* (3): $f = 0.25$ and (D) *Case* (4): $f = 0.5$.

and 3.16). However, the distribution of stresses σ^*_{11}, σ^*_{33} and σ^*_{21} is strongly non-linear across the wall shear zone, Figs. 4(c), 5(c), 6(a, c) and 7(c). A comparison between σ^*_{12} and σ^*_{21} demonstrates that the stress tensor is asymmetric in the Cosserat continuum except for the conditions in which $\partial m^*_2/\partial x_2 = 0$, Figs. 6(a, b) and 7(a, b). The latter states occur at two positions with $\sigma^*_{21} = \sigma^*_{12}$ which correspond to the extrema of m^*_2. This can be distinguished by comparing Fig. 4(b) with Fig. 6(b, c), and Fig. 5(b) with Fig. 7(b, c) for CP and CV conditions, respectively.

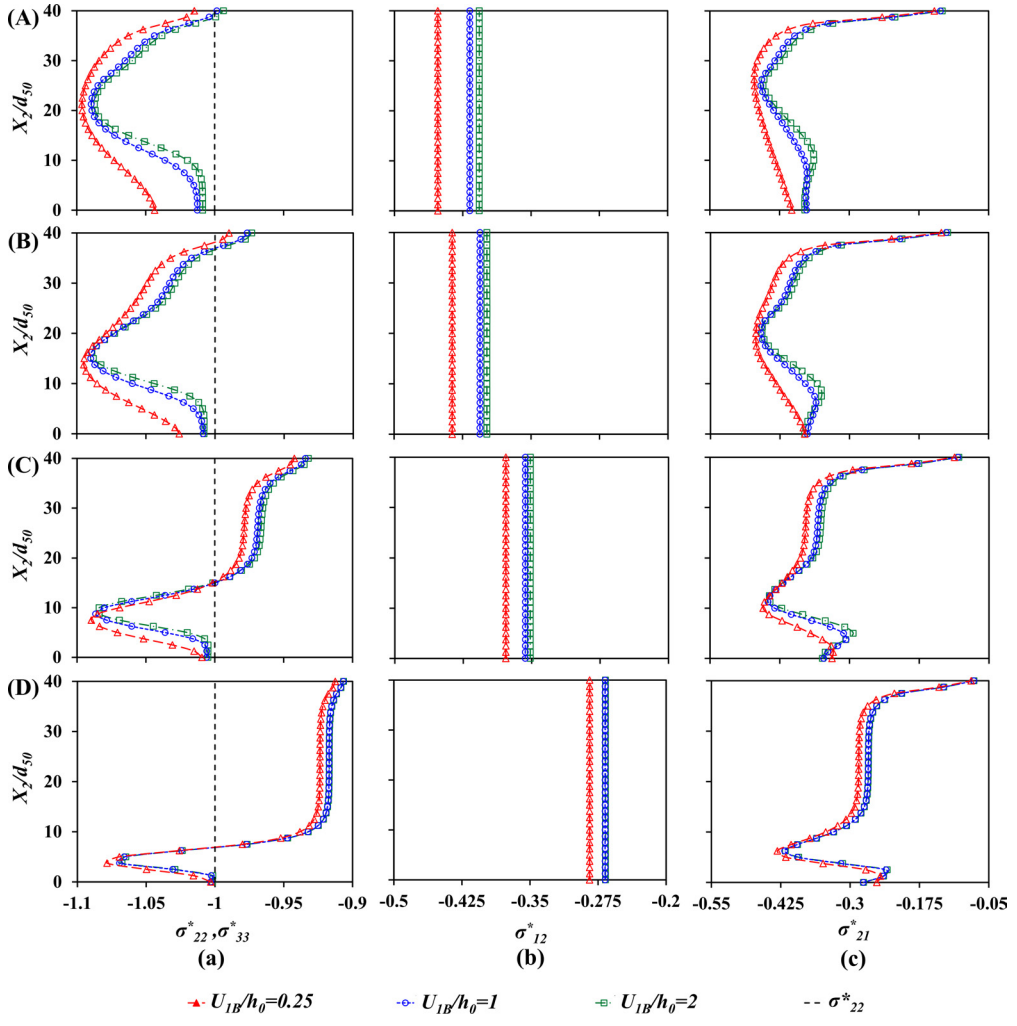

Fig. 6. Variation of (a) σ^*_{22}, σ^*_{33}, (b) σ^*_{12} and (c) σ^*_{21}, across X_2/d_{50} at different U_{1B}/h_0 in CP shearing for: (A) *Case* (1): $f = 0.05$, (B) *Case* (2): $f = 0.10$, (C) *Case* (3): $f = 0.25$ and (D) *Case* (4): $f = 0.5$.

Independent of the assumed Cosserat boundary conditions, the normal stresses in the center of the wall shear zone approach to a similar stationary state, which is acquired from the classical elasto-plastic Lade's material under shearing, i.e., $\sigma^*_{11} = \sigma^*_{22} = \sigma^*_{33}$. Stresses and couple stresses are extrema at the shear zone edges, and showing pronounced rises, Figs. 4(b, c), 5(b, c), 6(a, c) and 7(c).

Wall roughness results in resistance mobilization and volume change inside the wall shear zone in both confining constraints, Figs. 8 and 9. In CP condi-

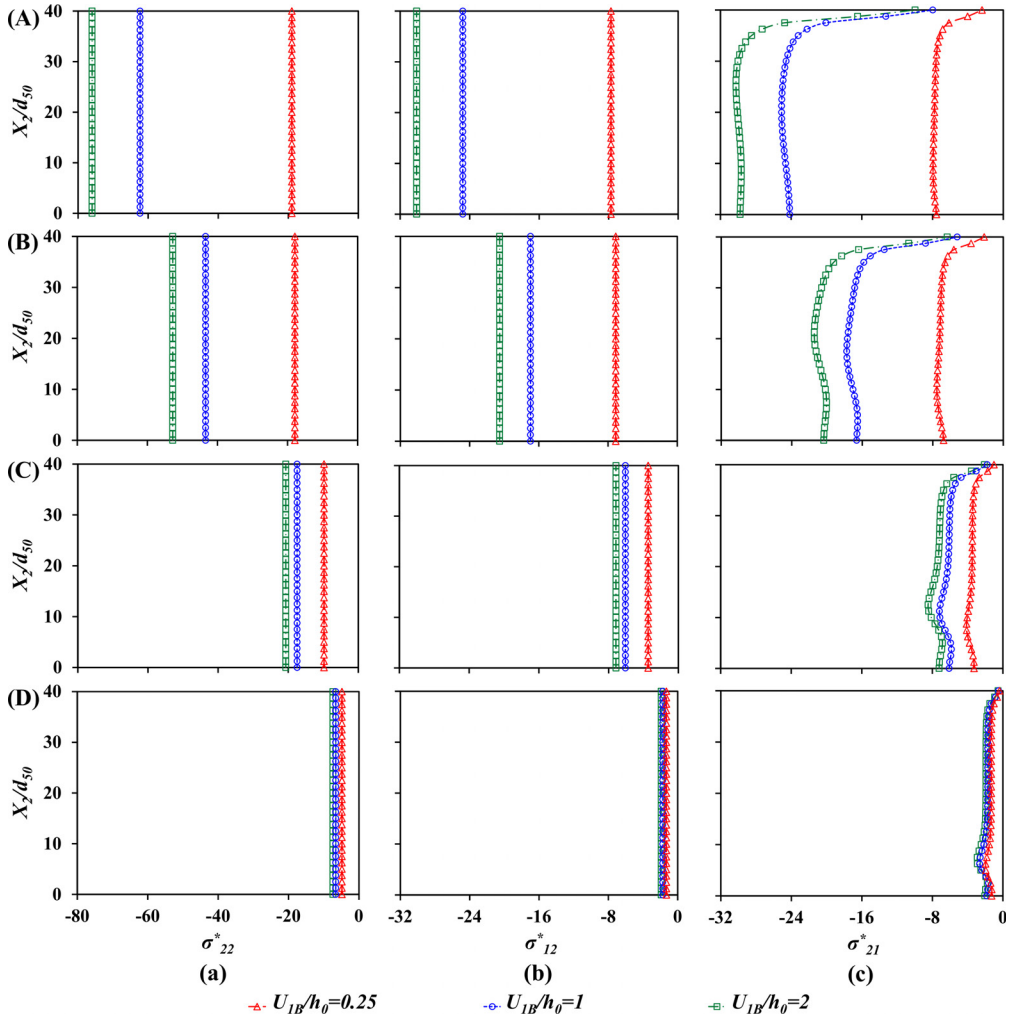

FIG. 7. Variation of (a) σ^*_{22}, (b) σ^*_{12} and (c) σ^*_{21}, across X_2/d_{50} at different U_{1B}/h_0 in CV shearing for: (A) *Case* (1): $f = 0.05$, (B) *Case* (2): $f = 0.10$, (C) *Case* (3): $f = 0.25$ and (D) *Case* (4): $f = 0.5$.

tion, continuous dilation is observed, with the largest dilation rate happening near the peak point and moving towards zero at the steady-state, Fig. 8(E). At the steady condition, the soil is continually deforming at a constant shear stress ratio and constant volume. In both normal confining constraints, the shear resistance increases when wall roughness grows. Higher normal and shear stresses are obtained for a lower interface coefficient (f_w), as given in Figs. 8(A–D) and 9(A–D) related to CP and CV conditions, respectively.

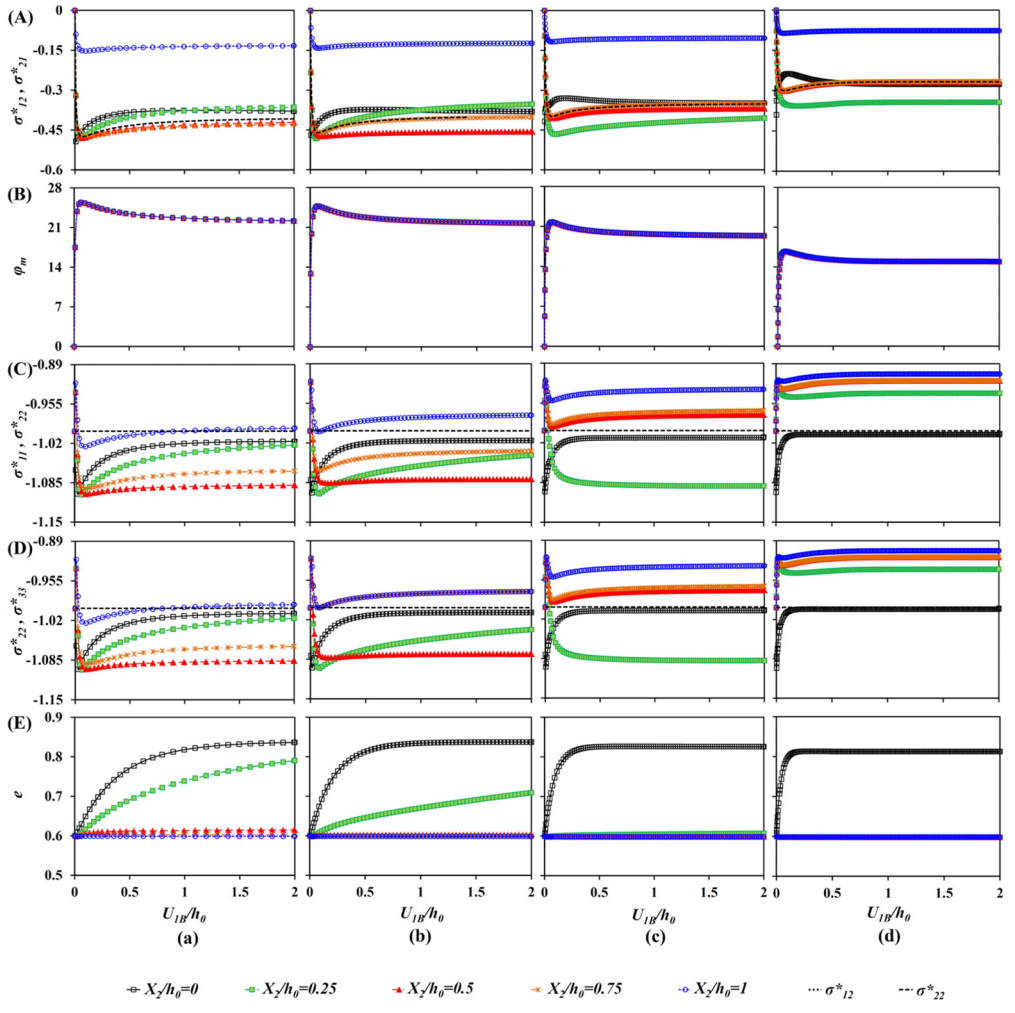

Fig. 8. Evolution of (A) σ^*_{12}, σ^*_{21}, (B) φ_m, (C) σ^*_{11}, σ^*_{22}, (D) σ^*_{22}, σ^*_{33} and (E) e at different X_2/h_0 in CP shearing for: (a) *Case* (1): $f = 0.05$, (b) *Case* (2): $f = 0.10$, (c) *Case* (3): $f = 0.25$ and (d) *Case* (4): $f = 0.5$.

The rough walls exhibit higher strength compared to the smooth ones, which is rational as the rough wall is more interlocked with the boundary particles and thus causes more resistance to shear than the smooth wall, Figs. 8(A) and 9(A). This fact is related to the amount of particle rearrangement that can happen. As the rougher wall has greater surface friction, the particles adjacent to the wall surface are not rearranged during continuous shearing as long as the shear stress is not sufficiently large to prevail over the inter-granular soil friction. Limiting particle rearrangement leads the interface to attain a steady condition at small

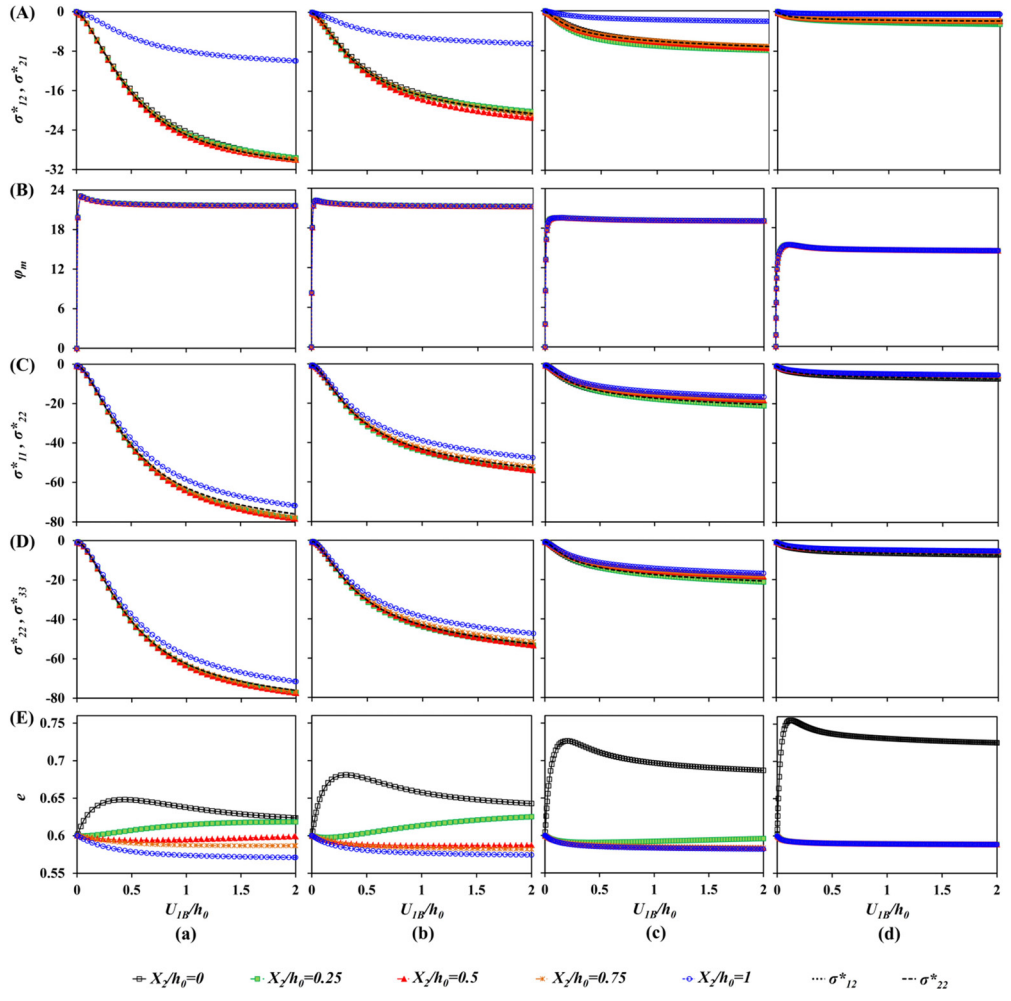

FIG. 9. Evolution of (A) σ^*_{12}, σ^*_{21}, (B) φ_m, (C) σ^*_{11}, σ^*_{22}, (D) σ^*_{22}, σ^*_{33} and (E) e at different X_2/h_0 in CV shearing for: (a) *Case* (1): $f = 0.05$, (b) *Case* (2): $f = 0.10$, (c) *Case* (3): $f = 0.25$ and (d) *Case* (4): $f = 0.5$.

deformation. Elastic perfect-plastic failure trend with negligible material dilation happens along the smooth walls, while shear localization with significant strain-softening and bulk dilatancy takes place along the rough walls, Figs. 8 and 9.

The evolution of frictional resistance at the bottom wall's surface can be defined by the stress ratio $(\sigma^*_{12}/\sigma^*_{22})$ or by the mobilized wall friction angle, φ_m, expressed as $\varphi_m = \tan^{-1}(\sigma^*_{12}/\sigma^*_{22})$. As σ^*_{22} is constant across the layer height, the variation curves for the wall friction angle are similar to those of the bounding wall shear stress, σ^*_{12}, Fig. 8(A, B). In CP condition, the mobilized

wall friction angle, φ_m, also illustrates an increasing trend up to a peak value, followed by subsequent post-peak strain-softening phase leading to a steady-state at higher shear deformations, Fig. 8(B). The latter state is also called the constant volume or critical state, and the corresponding friction angle is mostly known as the constant volume friction angle. As shown in Figs. 8(B) and 9(B), the mobilized peak wall friction angle is 25.43° and 23.08°, 24.72° and 22.16°, 21.77° and 19.58°, 16.72° and 15.19° in CP and CV conditions, respectively, for $f_w = 0.05$, 0.10, 0.25 and 0.50, respectively. While, the mobilized residual wall friction angle is 22.15° and 21.62°, 21.73° and 21.26°, 19.38° and 19.10°, 14.95° and 14.83° in CP and CV conditions, respectively, for $f_w = 0.05$, 0.10, 0.25 and 0.50, respectively. The constant volume friction angle represents the lowest shear resistance of the material [28]. Similar to shearing under CP, the asymptotical values of wall friction angle in CV shearing increase as f_w decreases, Fig. 9(B). Comparing the magnitudes of the wall friction angle obtained from CP and CV shearing exhibits that, while more noticeable peaks are obtained for CP condition, the rather same residual values are reached for the same coefficient f_w in both confining constraints. This implies that the peak values of the wall friction angle are affected by the stress induced inside the soil body, but the residual values do not depend on the stress level. These findings also suggest that the wall roughness effect can be appropriately reflected by the boundary constraint between the micro-rotation and the shear displacement with the coefficient f_w, as given in the relation (3.11).

Regarding the above values of wall friction angle, the mobilized peak and residual values in $f_w = 0.05$, 0.10, 0.25, and 0.50 decrease almost linearly as f_w increases. It has been shown that the mobilized wall friction angle changes in the range of 0° to 26.5° with rising wall roughness [37]. The latter magnitude is the internal friction angle of the medium dense fine silica sand. It is noteworthy that the magnitudes of wall friction angles obtained for the selected materials are smaller than those of typical ones [71, 72]. However, it should not be overlooked that the above friction values have been obtained for a medium dense fine silica sand in contact with rough, medium rough, and relatively smooth walls. On the other hand, the peak and residual friction angles are also dependent on several parameters such as stress level, size, shape, and surface roughness of particles, initial density of granular material, surface roughness, and stiffness of bounding structure.

The difference between the peak and the residual wall friction angles is around 3.28° and 1.46°, 2.99° and 0.90°, 2.39° and 0.48°, 1.77° and 0.36° in CP and CV conditions, respectively, for $f_w = 0.05$, 0.10, 0.25, and 0.50, respectively. This shows that the material softening rate decreases with f_w increasing or wall roughness decreasing. However, this rate is not severe for the range of wall roughness considered.

Figure 8(E) demonstrates the evolution of the void ratio at different levels across the soil layer under CP shearing. The wall shear zone displays a pronounced dilation after a primary compaction. On the contrary, the density of granular material exterior to the wall shear zone ceases to vary after an initial increase [14]. In the middle of the localized deformation zone, the volumetric strain is compressive at the start of shearing, then well before the peak, the layer begins dilating, while tending towards a constant value at large displacement. However, the evolution curves of void ratio deviate from each other before the peak stress is reached. Eventually, the dilation rate tends to zero, and the void ratio-displacement curves will be nearly horizontal [14]. External to the wall shear zone, the void ratio slightly increases and is almost steady for continuous shearing. This indicates that for an advanced shearing, the soil material outside the wall shear zone behaves as a rigid body after the peak. The dilatancy characteristics become larger with an increase in wall roughness, as indicated in Fig. 8(E). The values of void ratio within the wall shear zone are about 0.84, 0.83, 0.82 and 0.81 for $f_w = 0.05$, 0.10, 0.25 and 0.50, respectively. However, the difference between these values is not severe with respect to the variation of the wall roughness. Nevertheless, it should be emphasized that no relative displacement occurs in the current FE simulations between the layer and the moving wall [69]. Consequently, the granular body is entirely sheared against the wall surface [31, 65, 73–75]. This means that no limitation on wall shear strength is taken into account, which causes infinite shear deformations within the granular body. In smooth walls, however, only a very limited narrow area adjacent to the moving wall is influenced, and the contribution of the rest parts of the layer is not significant. In such roughness conditions, the shear zone occurs with extremely smaller width and more localization intensity comparing to that of medium rough and rough walls. Accordingly, the polar variables, such as increasing void ratios, Cosserat couple stresses and rotations are greater and more pronounced close to smooth walls due to the very smaller shear zone width. This also corresponds to the former numerical studies in this area [1, 43]. Moreover, the variation pattern of void ratio, shown in Figs. 2(c) and 8(E), is directly dependent on the shear zone location as well as the position of the particular elements considered across the layer height ($x_2/h_0 = 0.00$, 0.25, 0.50, 0.75, 1.00). These elements are not necessarily located at the middle or edge of the localized shear zone as their locations are changing with respect to the wall roughness and the shearing mechanism.

For shearing under CV condition, the void ratio interior to the wall shear zone rises first to a peak value, which is lower than the corresponding value in CP condition, and then continually decreases as the applied shear displacement increases, comparing Figs. 8(E) and 9(E). Nevertheless, the void ratio out of the wall shear zone decreases continuously from the beginning of shearing, Fig. 9(E).

The normal dilation at the critical state decreases with a decrease of normalized roughness, r_w/d_{50}. As represented in Fig. 9(C, D), the difference between two confining constraints may be related to the continuous increase of pressure in CV condition resulting from localized dilation [14]. According to Figs. 8 and 9, under a different normal confining condition, the granular layer will have a different tendency of deformation, such as dilation and contraction, which affects the variation of volume and normal stress [14].

The deformed soil layer with contour plot of void ratio in the residual state ($u_{1B} = 2.00h_0$) and for different values of f_w is presented in Figs. 10 and 11 for CP and CV shearing, respectively. The shear deformations are horizontally localized and in direct contact with the bottom wall. The red strip shows higher void ratios due to material dilatancy in the wall shear zone. When the wall roughness

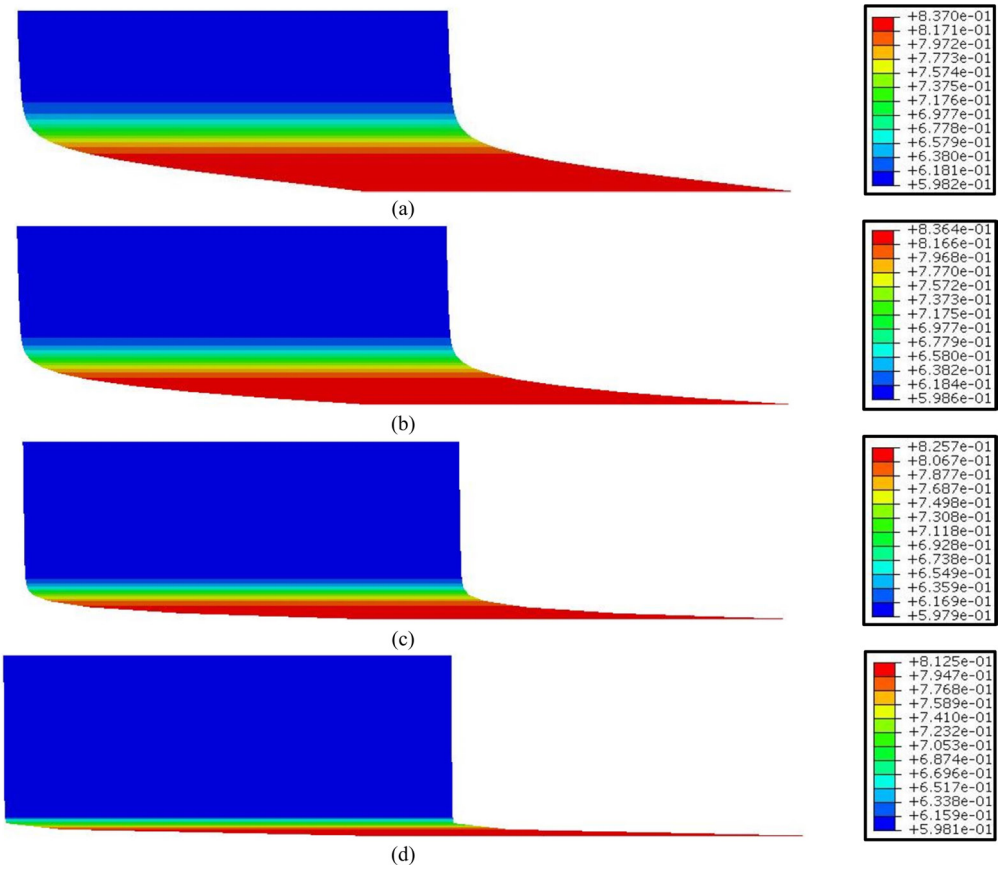

Fig. 10. Contour plot of void ratio in deformed configuration of granular soil layer after $U_{1B}/h_0 = 2.00$ in CP shearing for: (a) *Case* (1): $f = 0.05$, (b) *Case* (2): $f = 0.10$, (c) *Case* (3): $f = 0.25$ and (d) *Case* (4): $f = 0.5$.

changes, it will strongly influence the mobilized shear resistance along the wall surface and the localization behavior. The shear zone width becomes larger with an increase of wall roughness. With a larger value for f_w, which corresponds to a higher ratio of micro-rotation to normalized shear movement along the wall, showing a relatively smooth surface condition, a more significant localization with a narrower width takes place. Conversely, a smaller value for f_w, which corresponds to a relatively rough surface condition, leads to a less localization with a larger thickness. In CP condition, the wall shear zone width predicted from the developments of void ratio, is about 19, 14, 9 and 4 times the intrinsic length scale for $f_w = 0.05$, 0.10, 0.25 and 0.50, respectively. However, the shear deformations occur in the entire section of the shear layer in touch with the rough interface under CV condition, which is distinguished from the distribution of

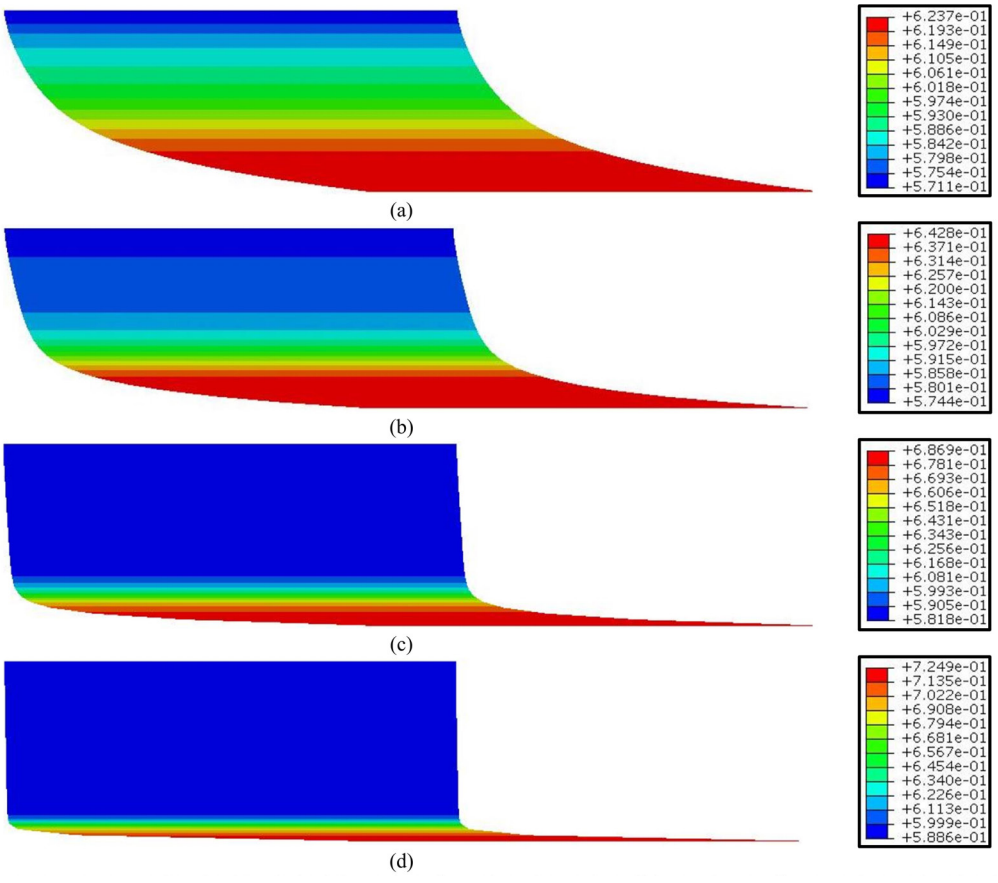

FIG. 11. Contour plot of void ratio in deformed configuration of granular soil layer after $U_{1B}/h_0 = 2.00$ in CV shearing for: (a) *Case* (1): $f = 0.05$, (b) *Case* (2): $f = 0.10$, (c) *Case* (3): $f = 0.25$ and (d) *Case* (4): $f = 0.5$.

the void ratio, Fig. 11(a). The localized deformations are more pronounced out of the wall shear zone in CV condition compared to that of CP condition. In particular, localization cannot be detected in the granular medium adjacent to a moving rough wall ($f_w = 0.05$) under CV condition up to a shear displacement of $U_{1B}/h_0 = 2.00$, Fig. 11(a). As a result, the computed width of the wall shear zone in CV condition is around 15, 10 and 5 times the intrinsic length scale for $f_w = 0.10$, 0.25 and 0.50, respectively. Although both factors of normal confining constraint and bounding wall roughness have notable influences on the deformation field formed within the layer, they have rather negligible influences on the evolution and location of the wall shear zone. In the majority of the considered cases, the localized zone has almost similar width for both CP and CV interface shearing with the same f_w value. It is found that the width of the wall shear zone is independent of the normal confining condition after applying large shear deformations.

4.2. The influences of pressure level and initial void ratio

Here, the impacts of pressure level (p_0) and initial void ratio (e_0) are explored on the variation of stress ratio ($\sigma^*_{12}/\sigma^*_{22}$) and the normalized width of the wall shear zone (w/d_{50}). For this purpose, different amounts of vertical pressure ($p_0 =$ 100, 500, 1000 kPa) and initial void ratio ($e_0 = 0.60$, 0.75, 0.90) are taken into account for a granular layer sheared against a bounding wall of varying surface roughness ($f_w = 0$, 0.05, 0.10, 0.25, 0.50, 1).

According to Fig. 12(aA, bA), larger pressures result in a smaller stress ratio at both peak and residual states in CP interface shearing. Correspondingly, softening is more evident at lower pressure levels. As previously discussed and also shown in Fig. 12(aA, bA), the magnitudes of peak and residual stress ratios significantly increase with a reduction of the interface coefficient, f_w. In addition, the normalized width of the wall shear zone slightly rises as the vertical pressure increases, Fig. 12(cA). In this regard, the higher values of shear zone width correspond to the lower values of f_w. Comparing the 3D surfaces in Fig. 12, it is revealed that the results of CP interface shearing under higher pressure levels tend towards those of CV condition. It can be stated that the maximum values of stress ratio increase with reducing the dilatancy constraint which is equal to a decrease in the pressure level.

Under both CP and CV confining conditions, the peak and residual stress ratios decrease when the initial void ratio increases, Fig. 12(aB, bB, aC, bC). It is seen in Fig. 12(cB, cC) that the normalized width of the wall shear zone grows with an increase of the initial void ratio. For very loose granular materials (i.e., $e_0 \geq e_c = 0.84$), the shear zone width is equivalent to the height of the shear layer (here, $40 \times d_{50}$). This means that the shear zone width attains the size

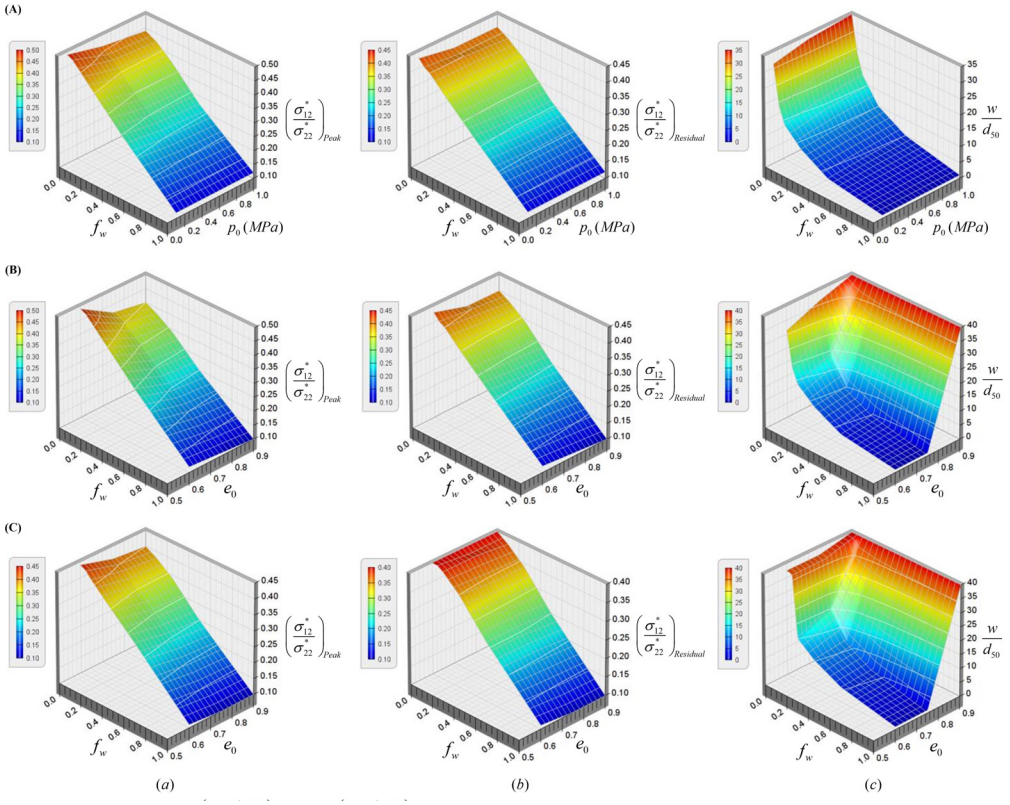

FIG. 12. Variation of (a) $(\sigma_{12}^*/\sigma_{22}^*)_{Peak}$, (b) $(\sigma_{12}^*/\sigma_{22}^*)_{Residual}$ and (c) (w/d_{50}) versus (A) p_0 and f_w and (B-C) e_0 and f_w in: (A-B) CP and (C) CV shearing.

of the granular medium in case the initial void ratio is equivalent to or greater than its critical value, i.e., $e_c = 0.84$. The extent of dilative response of granular materials under shearing which is determined by an increase of the void ratio grows with a decrease of both applied pressure level and initial void ratio.

4.3. DEM-based simulations

DEM, first proposed by Cundall (1979), is one of the efficient methods to properly investigate the micro-mechanical behavior of granular media [76]. A number of DEM studies has been carried out to consider the interface shear response of granular materials [19, 67, 68, 77–88].

In this section, the shear behavior of a granulate-continuum interface system is examined from a micro-mechanical perspective, Fig. 13. To this end, DEM-based simulations of the interface shear test under CP and CV conditions are carried out using 3D particle flow code, PFC^{3D} [89]. In this regard, the granular

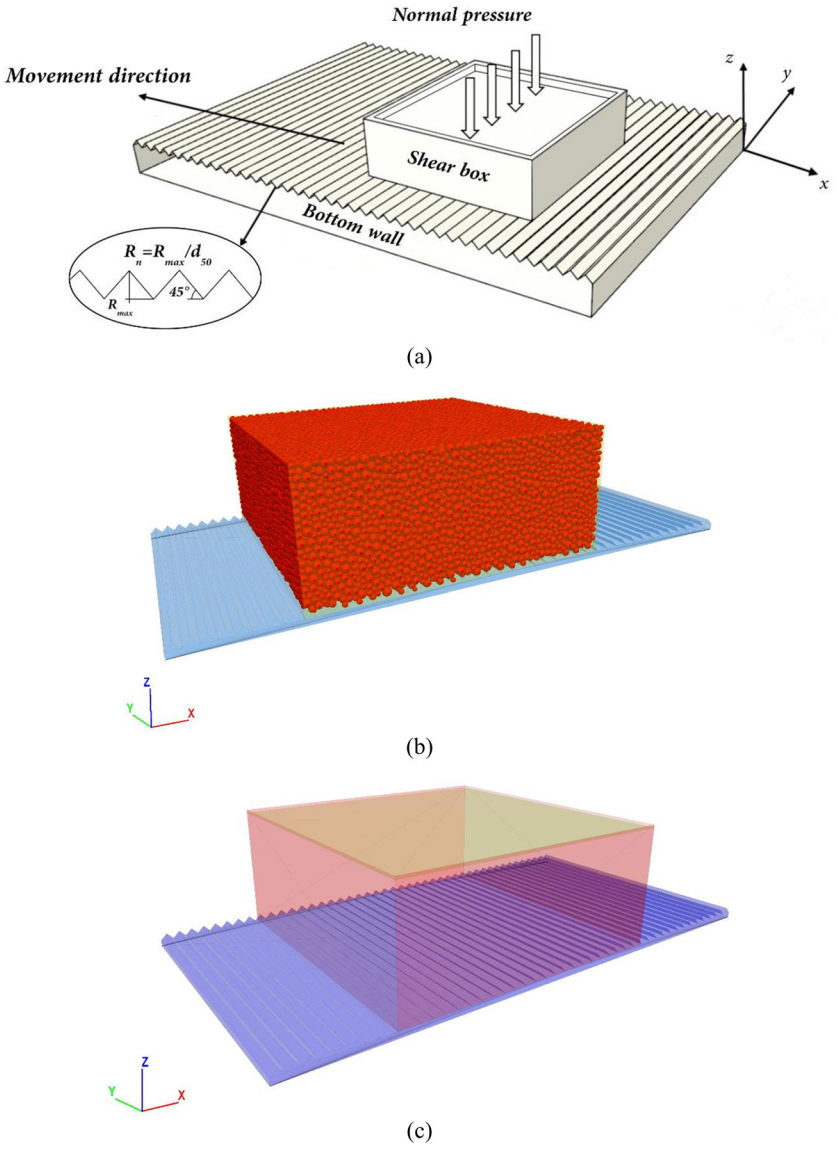

Fig. 13. 3D DEM model of interface shearing: (a) schematic view of an interface shear test, (b) an assembly of spherical particles forming granular specimen in contact with moving bottom wall of varying surface roughness, and (c) rigid interface shear box composed of four fixed sidewalls, one top wall moving in the z-direction and one bottom wall moving in the negative x-direction.

specimen is created by an assembly of rigid spherical particles with different sizes in the range of (0.5–1.5) mm and with an average size of $d_{50} = 1.0$ mm. The specimen has a length and width of 100 mm and a height of 40 mm ($l \times b \times h_0 =$

$100 \times 100 \times 40\,\mathrm{mm}^3$), Fig. 13(a). About 55000 particles are produced to form the specimen, which is placed within the interface shear box consisting of four rigid sidewalls and bounded by upper and lower horizontal walls, as displayed in Fig. 13(b, c). The normal pressure is exerted on the top surface of the specimen via the upper wall, and the shear displacement is applied to the bottom surface of the specimen by moving the lower wall. The surface roughness of the lower wall is modeled by a regular arrangement of microscopic teeth. Each tooth is configured by two side segments inclining alternatively 45° and 135° with respect to the Z-axis, as schematically shown in Fig. 13(a). As previously presented in Section 3, normalized or relative roughness, $R_n = R_{max}/d_{50}$, is utilized to specify the roughness condition of the lower wall surface. R_{max} is the vertical distance from peak to valley of the asperities along the wall's surface [65].

DEM simulations of the interface shear test are performed in three stages. At first, the particles are randomly generated in the shear box to form a dense specimen with an initial porosity of $n_0 = 0.32$. At the second stage and for shearing under CP condition, the normal load is imposed and maintained on the upper wall, which moves uniformly in the vertical direction. In contrast, the vertical movement of the upper wall is constrained at the second stage for shearing under CV condition. Eventually, at the third stage, the lower wall moves to the left at a constant horizontal velocity of 0.12 mm/min to ultimately achieve a shear movement of $U_{XB} = 12\,\mathrm{mm}$, while the shear box is fixed in space. The ratio of mean unbalanced force to mean contact force is controlled to fulfill a quasi-static interface shearing. Correspondingly, each time-step takes about 10^{-5} s during shear loading that guarantees a quasi-static condition.

DEM calculations are based on two rules: Newton's second law, which applies to particles, and the force-displacement law, which applies to particle contacts. Here, the force-displacement relationship between particles follows the linear frictional contact model with rotation resistance. In this model, contact forces vary linearly with the relative displacement of particles in contact to prevent slipping. Slippage happens when the contact forces reach the Coulomb failure limit. Correspondingly, rotation causes a relative rotation between two particles in contact. The contact moments increase linearly with the relative cumulative rotation at particle contacts. In DEM analyses, the energy dissipation by the frictional sliding is not sufficient to have a stable condition due to the dynamic formulation of the model. Thus, additional dissipation is incorporated by using a local damping factor of 0.7, as proposed in PFC^{3D} for quasi-static problems [89]. The input parameters of DEM simulations are listed in Table 2.

Here, the impacts of bottom wall roughness, pressure level, and normal confining constraints are explored on the microscopic and macroscopic responses of the granular specimen under shearing. In this regard, a series of DEM simulations is carried out under CP and CV conditions with different values of wall

Table 2. Input parameters used in DEM simulations.

Description	DEM parameters	Value
Number of particles		55000
Density (kg/m^3)		2650
Mean particle diameter (mm)	d_{50}	1.00
Initial porosity	n_0	0.32
Inter-particle normal-to-shear stiffness ratio	k_n/k_t	2.00
Inter–particle frictional coefficient	f_p	0.24
Particle–lateral walls frictional coefficient	f_{pw}	0.50
Particle–bottom wall frictional coefficient	f_{pbw}	0.01
Inter-particle rolling resistance coefficient	μ_r	0.05
Damping coefficient		0.70

roughness (R_n = 0.0, 0.5, 1.0, and 2.0), indicating smooth, relatively smooth, rough, and very rough walls. Moreover, different pressure levels (p_0 = 100, 200, 500, 1000, and 1800 kPa) are applied at the second stage of each simulation. For verification purposes, the values of the applied pressure level have been increased to determine the pressure at which the CP results approach those of CV, regardless of the grain crushing phenomenon.

Unlike the lateral infinite shear layer, the deformation and stress fields are heterogeneous within the granular specimen due to the presence of the rigid sidewalls of the interface shear box. For this reason, DEM results and FE predictions cannot be compared quantitatively, and instead, qualitative comparisons are provided. In order to minimize the influence of the lateral boundaries of the shear box on the DEM results, the variation of field variables and state quantities are recorded in the mid-section of the granular specimen farther away from the rigid lateral boundaries.

Despite the fact that the granular medium is simulated by an assembly of spherical particles in DEM, the field quantities can be computed in an average sense within the representative element volumes (REVs) called measuring spheres. To this end, the center of each measuring sphere is assigned to a particular point in which the continuum field quantities are to be computed. Here, the measuring sphere size is selected to be $5 \times d_{50}$. In the present study, the average of stress components is computed over a measuring sphere based on the method suggested in [90].

The variation of field quantities obtained from DEM simulations are presented across the normalized height (Z/d_{50}) of the granular specimen under CP and CV shearing conditions, as shown in Figs. 14–17. All figures are illustrated for an applied wall displacement of 12 mm ($U_{XB}/h_0 = 0.30$).

Particle movement can properly be traced in DEM simulation. According to Figs. 14(a) and 15(a), the normalized horizontal displacement, u_x/h_0, is local-

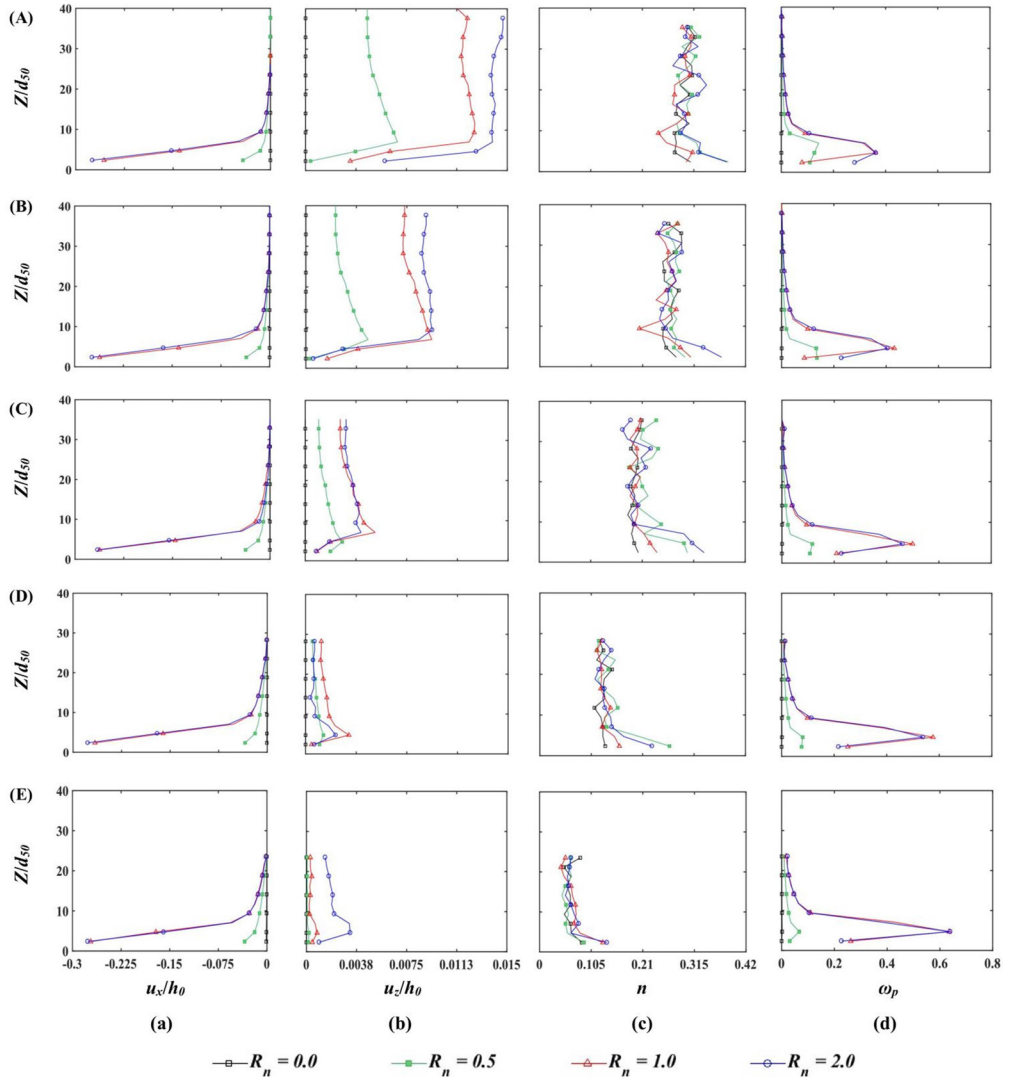

FIG. 14. Variation of (a) u_x/h_0, (b) u_z/h_0, (c) n and (d) ω_p across Z/d_{50} in CP shearing with different R_n values after $U_{XB}/h_0 = 0.3$ for: (A) $p_0 = 100\,\text{kPa}$, (B) $p_0 = 200\,\text{kPa}$, (C) $p_0 = 500\,\text{kPa}$, (D) $p_0 = 1000\,\text{kPa}$ and (E) $p_0 = 1800\,\text{kPa}$.

ized into a narrower zone near the bottom wall when its roughness increases. The gradient of horizontal displacement in this zone decreases with decreasing wall roughness. As observed in the figures, the particles closer to the moving wall have larger horizontal displacements forming a wall shear zone. It is seen in Figs. 14(aA,aB) and 15(aA,aB) that the horizontal displacement decreases substantially with increasing distance from the bottom wall, especially in the

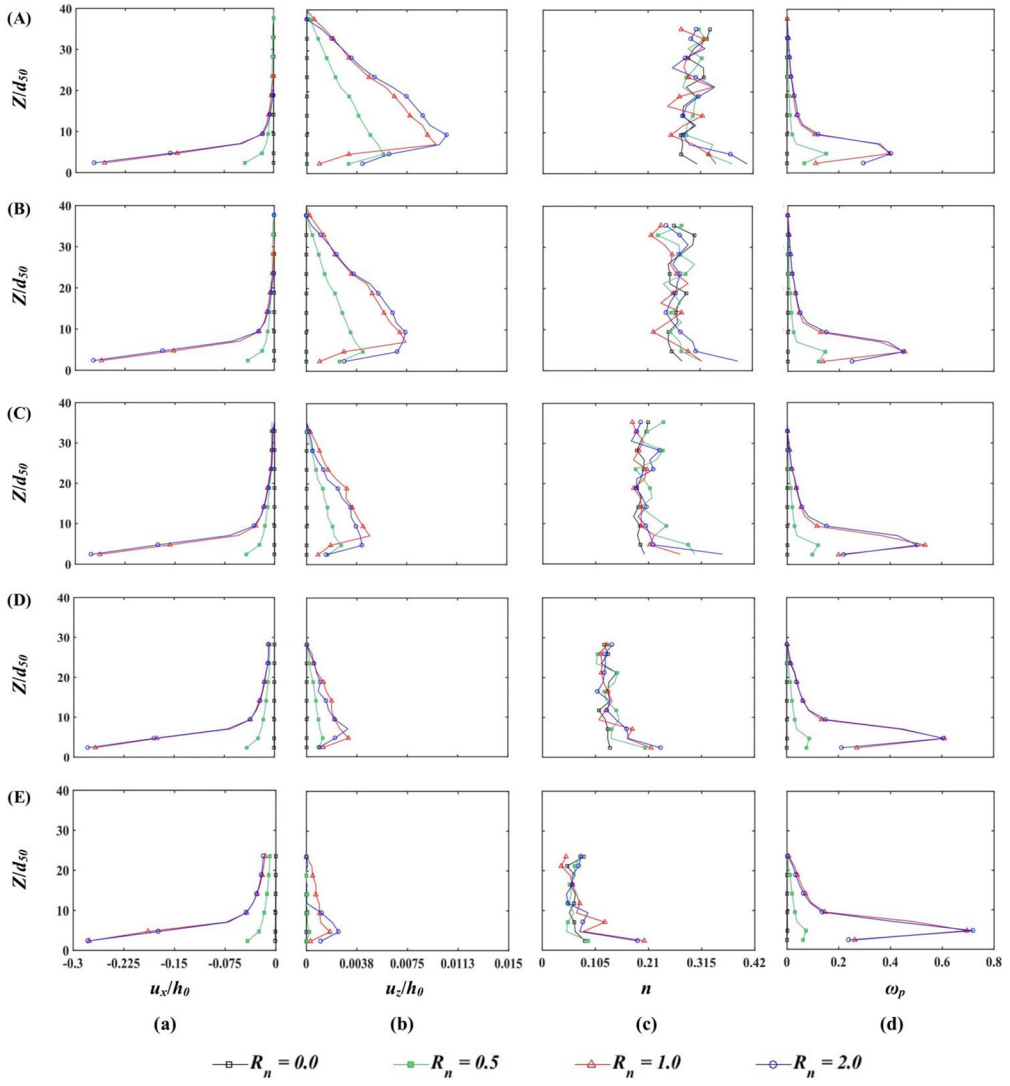

Fig. 15. Variation of (a) u_x/h_0, (b) u_z/h_0, (c) n and (d) ω_p across Z/d_{50} in CV shearing with different R_n values after $U_{XB}/h_0 = 0.3$ for: (A) $p_0 = 100\,\text{kPa}$, (B) $p_0 = 200\,\text{kPa}$, (C) $p_0 = 500\,\text{kPa}$, (D) $p_0 = 1000\,\text{kPa}$ and (E) $p_0 = 1800\,\text{kPa}$.

cases under lower pressure levels (i.e., $P_0 = 100$, and $200\,\text{kPa}$). In the mentioned cases, the horizontal displacement approaches nearly zero at parts far from the moving bottom wall. On the contrary, the progression of the horizontal displacement outside the wall shear zone is more evident at higher pressure levels (i.e., $P_0 = 500$, 1000, and $1800\,\text{kPa}$) due to more interaction of particles within the specimen, Figs. 14(aC, aD, aE) and 15(aC, aD, aE). It is revealed by comparing

Figs. 14(a) and 15(a) that the evolution of horizontal displacement farther from the bottom wall is more significant in CV condition than that of CP condition. This result was also certified previously in Figs. 2(a) and 3(a) relevant to the Cosserat FE calculations.

The variation of vertical displacement, u_z/h_0, within the granular specimen can change considerably with respect to the wall roughness, Figs. 14(b) and 15(b). When free dilatancy is allowed, as in the case of shearing under CP condition, the granular specimen height can change in the vertical direction, Z, due to dilatant or contractant behavior of the material, as also shown in Fig. 14(b). The vertical deformations above the wall shear zone in the CP condition, which illustrate the continuous material dilation, have a negligible displacement gradient that confirms the granular specimen is monotonously moving away from the bottom wall, such as a rigid body. Opposed to the CP shearing, the height of the granular specimen under CV shearing is fixed, Fig. 15(b). The above trend was similarly observed in the obtained FE results, shown in Figs. 2(b) and 3(b).

The normalized displacement fields, u_x/h_0, and u_z/h_0, interior to the granular specimen, obtained from the current DEM approach, have non-linear trends, similar to the Cosserat FE results, comparing Figs. 2(a, b) and 3(a, b) with Figs. 14(a, b) and 15(a, b). The non-linear variation of the curves also demostrates the formation of a shear zone along the bottom wall's surface. DEM results show that the interface behavior is significantly affected by the wall roughness, seen in the Cosserat FE simulations as well.

As a typical response of a densely packed granular assembly under CP shearing, the dilation is observed inside the localized shear zone along the wall, Fig. 14(c). However, dilatancy in the wall shear zone results in contractancy in the remaining parts of the granular specimen under CV shearing, Fig. 15(c). Therefore, the requirement for CV condition is satisfied within the whole specimen.

Porosity possesses the most significant magnitudes inside the wall shear zone for varying values of the wall roughness, Figs. 14(c) and 15(c). As shown in the figures, the values of porosity outside the wall shear zone are much smaller than its primary magnitude ($n = 0.32$) owing to the application of different amounts of initial normal pressure. The presence of a relatively smooth wall (i.e., $R_n = 0.5$) in touch with the granular specimen results in very low volume changes. In this regard, volume increase does not effectively contribute to the shear strength of the relatively smooth wall, even in dense granular bodies, as observed in Figs. 14(c) and 15(c). This implies that the triggered shear stress is not adequately large to affect a great portion of the granular specimen in contact with a relatively smooth wall under motion due to the minimum interlocking between the boundary particles and the wall's surface. As the wall

roughness increases, dilatancy and volume change of the granular body become more evident, Figs. 14(c) and 15(c).

According to Figs. 14(d) and 15(d), non-linear variation of particle rotation, ω_p, with larger values at the lower surface of the granular medium close to the moving wall is manifested in both CP and CV conditions after a large shear movement of $U_{XB}/h_0 = 0.30$. The variations are in accordance with the distributions of particle displacement and volume change plotted in Figs. 14(a, c) and 15(a, c). The maximum values of particle rotation, accompanied by dilatancy, demonstrate where shear banding may be initiated under shearing. As the wall roughness increases, particle rotation also increases inside the wall shear zone and remains almost unchanged outside it, Figs. 14(d) and 15(d). The progression of particle rotation exterior to the wall shear zone almost ceases when the shear displacement is concentrated.

Under both CP and CV shearing, the particle rotation in the wall shear zone decreases for the relatively smooth wall (i.e., $R_n = 0.5$) as the applied pressure level rises. In contrast, it increases with an increase of pressure level for higher roughness values (i.e., $R_n = 1.0,\ 2.0$), as also seen in [67]. The reason for this irregular variation may be attributed to the normal and tangential forces and tangential moments acting on the inclined side segments of each tooth along the wall surface [67]. When the bottom wall moves to the left, it creates a clockwise particle rotation. As the wall roughness increases, the tooth height rises, and the interaction between the surface asperities and the boundary particles increases. Due to the friction prescribed between the inclined side segments of each tooth and the boundary particles, when the particles want to rotate and slide along the side segments, frictional forces are created in the opposite direction of their movement, which in turn leads to clockwise moments, which intensify the previous clockwise rotation of each particle. Consequently, the particle rotation increases in rougher walls ($R_n = 1.0,\ 2.0$) as the applied pressure level grows.

One way to find the width of the wall shear zone is to calculate the threshold limit of the curvature function for the mean particle displacement [82]. For this purpose, a best-fitting curve that passes through the most points of the average displacement versus height is determined and then the curvature function of the obtained curve is computed. Jing *et al.* [82], suggested that the threshold of the point of curvature is the height where the curvature function has a value equal to 0.02. Thus, with reference to the horizontal displacement profiles indicated in Figs. 14(a) and 15(a), the width of the wall shear zone formed in the vicinity of the bottom wall is about $2.9d_{50}$, $7.0d_{50}$, and $7.2d_{50}$ for relatively smooth, rough, and very rough surface conditions, respectively. Nevertheless, the effect of pressure level on the width of the wall shear zone is not remarkable. It is worth noting that this finding is reliable as long as the particle crushing is not taken

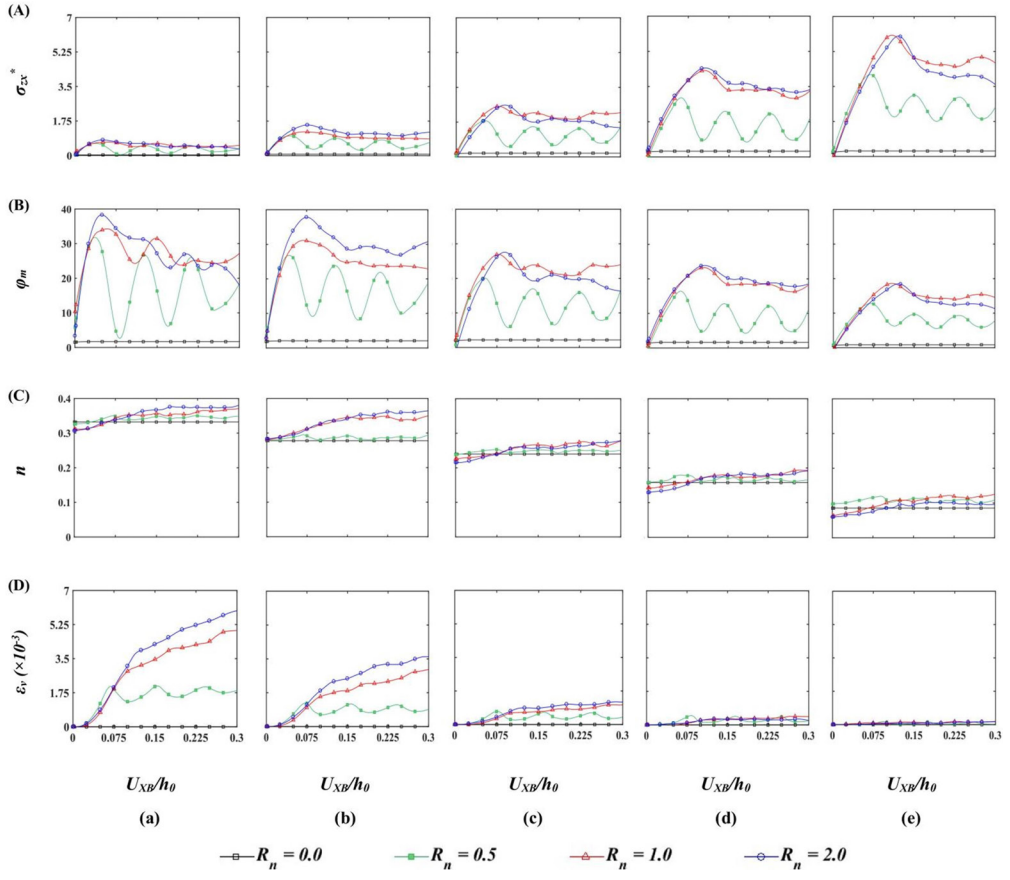

FIG. 16. Evolution of (A) σ^*_{zx}, (B) φ_m, (C) n and (D) ε_v across Z/d_{50} in CP shearing with different R_n values for: (a) $p_0 = 100\,\text{kPa}$, (b) $p_0 = 200\,\text{kPa}$, (c) $p_0 = 500\,\text{kPa}$, (d) $p_0 = 1000\,\text{kPa}$ and (e) $p_0 = 1800\,\text{kPa}$.

into account, particularly at higher pressure levels, similar to the current DEM simulations.

It is shown that the distribution of considered parameters across the height of the granular specimen is strongly influenced by the wall roughness and the applied pressure level, Figs. 14 and 15. However, the results relevant to rough and very rough walls ($R_n = 1.0$, 2.0) are comparable and very close to each other.

By comparing the obtained DEM results with the Cosserat FE predictions, it is found that they qualitatively correspond to each other.

According to Figs. 16(A) and 17(A), the wall roughness and the applied pressure level have controlling influences on the evolution of wall shear stress, σ^*_{zx}, mobilized at the middle of the bottom wall's surface in both normal confining conditions. In this regard, the rougher walls are resisting against larger shear

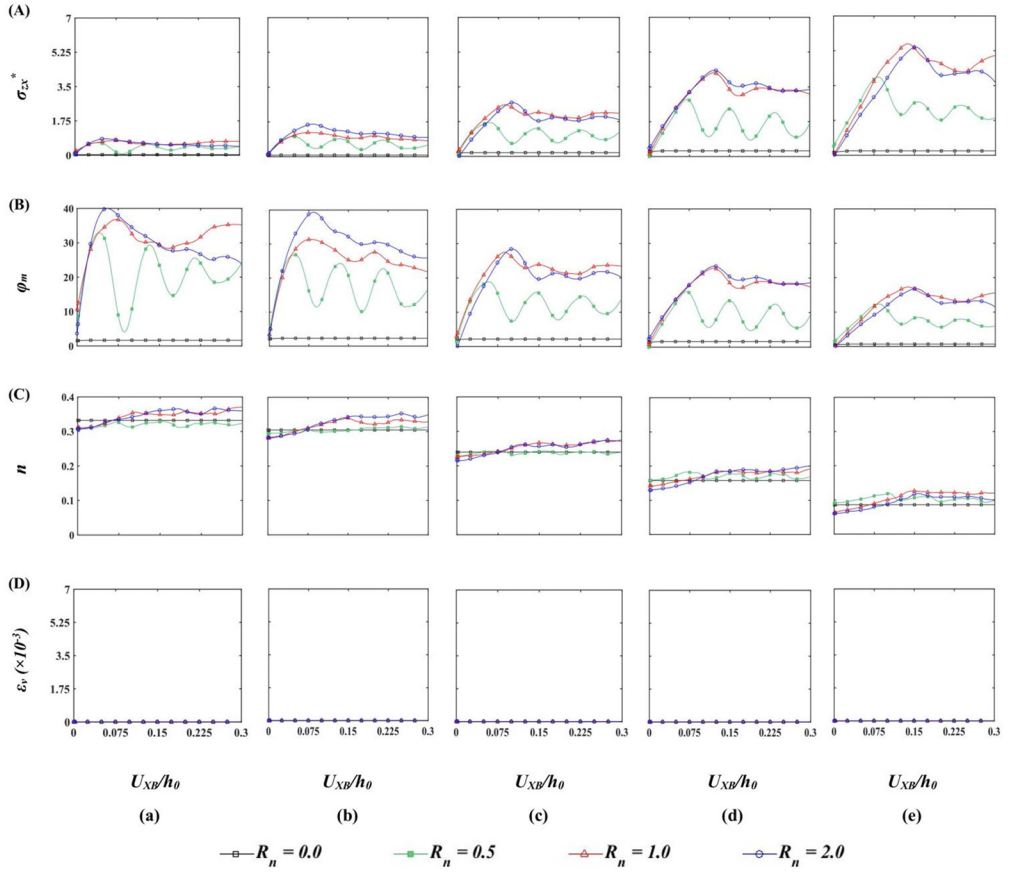

Fig. 17. Evolution of (A) σ^*_{zx}, (B) φ_m, (C) n and (D) ε_v across Z/d_{50} in CV shearing with different R_n values for: (a) $p_0 = 100$ kPa, (b) $p_0 = 200$ kPa, (c) $p_0 = 500$ kPa, (d) $p_0 = 1000$ kPa and (e) $p_0 = 1800$ kPa.

displacement, in comparison with smooth walls, because of sustaining the greatest stress ratios and completely mobilizing the shear resistance of the granular material. In addition, the peak values of the wall shear stress are obtained at larger shear displacements under both confining conditions as the pressure level increases, Figs. 16(A) and 17(A).

In response to the higher values of wall roughness (i.e., $R_n = 1.0, 2.0$), which corresponds to rough and very rough walls, close values of shear stresses at both peak, and stationary conditions are obtained. The evolution curves presented for rough and very rough walls possess more obvious peaks compared to that of relatively smooth wall, Figs. 16(A) and 17(A). For walls with higher roughness, all evolution curves of shear stress versus shear displacement first ascend to peak stress higher than the limit stress. Subsequently, they descend steadily and pro-

ceed towards asymptotic values under steady stress condition at large shearing, Figs. 16(A) and 17(A). As observed in the figures, the evolution curves of shear stress mobilized along the smooth wall result in perfectly plastic behaviors with no apparent peaks.

According to Figs. 16(B) and 17(B), similar to shear stress, the friction angle, $\varphi_m = \tan^{-1}(\sigma^*_{zx}/\sigma^*_{zz})$, mobilized at the middle of the bottom wall's surface increases first up to a peak state, and then it gradually softens and reduces towards a stationary value. The shear displacement in which the peak wall frictional resistance is taken place, increases in both CP and CV conditions as the wall roughness, and the pressure level rises, Figs. 16(B) and 17(B). The higher the pressure level, the lower the shear resistance. Concerning the wall friction angles, the mobilized peak and residual values increase almost linearly in both normal confining conditions when the wall roughness grows. It is observed that the mobilized wall friction angle rises in the range of around 0° to 40° with increasing wall roughness, Figs. 16(B) and 17(B).

Periodic fluctuations appear in the evolution curves of wall shear stress and wall friction angle during steady-state condition for $R_n = 0.5$, Figs. 16(A,B) and 17(A,B). This is due to that the layer of boundary particles cannot fit into the surface teeth. Therefore, they move in alternating order between the peaks and the valleys of the teeth, which results in periodic oscillation. In contrast, the layer of boundary particles can be trapped in the areas between the teeth of the wall surface in higher roughness values ($R_n = 1.0$, 2.0). In the latter cases, the layer of boundary particles travel with the moving wall, and no oscillation is observed in the evolution curves [82].

It is seen in Figs. 16(C) and 17(C) that all evolution curves of porosity, n, obtained at the middle of the bottom wall's surface, start at a certain value that is smaller than its primary magnitude ($n_0 = 0.32$). Then, the porosity curves continuously increase concerning the walls with higher surface roughness values (i.e., $R_n = 1.0$, 2.0), and subsequently, they approach asymptotical states at large shearing in both normal confinements, Figs. 16(C) and 17(C). This means that the granular materials contract first by applying the initial normal pressure and then dilate with advanced shearing. However, the porosity values in shearing under CV condition are lower than those in the corresponding CP condition, Figs. 16(C) and 17(C). Moreover, an isotropic specimen becomes anisotropic due to shearing. Continuous dilatancy takes place with the highest rate close to the peak stress which will be negligible at the steady-state, Figs. 16(C) and 17(C). For lower magnitudes of wall roughness (i.e., $R_n = 0.5$), the porosity insignificantly rises and is nearly steady for continued shear displacement. In smooth wall (i.e., $R_n = 0.0$), however, they remain zero during interface shearing.

Volumetric strain curves calculated for the whole specimen show the behavior similar to that of porosity in CP condition, Fig. 16(D). It is worth noting that

volumetric strain is calculated by the normal deformation of the specimen divided by its initial height. The volumetric strain starts rising, while tending towards

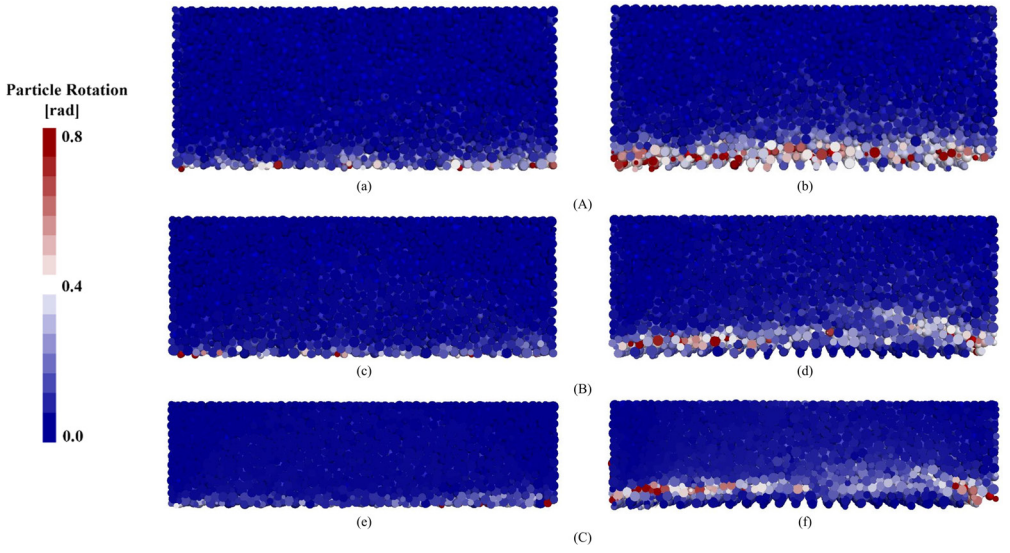

Fig. 18. Distribution of particle rotation within the deformed granular specimen under CP shearing with (a, c, e) $R_n = 0.5$ and (b, d, f) $R_n = 2.0$ after $U_{XB}/h_0 = 0.3$ and for: (A) $p_0 = 100\,\text{kPa}$, (B) $p_0 = 500\,\text{kPa}$ and (C) $p_0 = 1800\,\text{kPa}$.

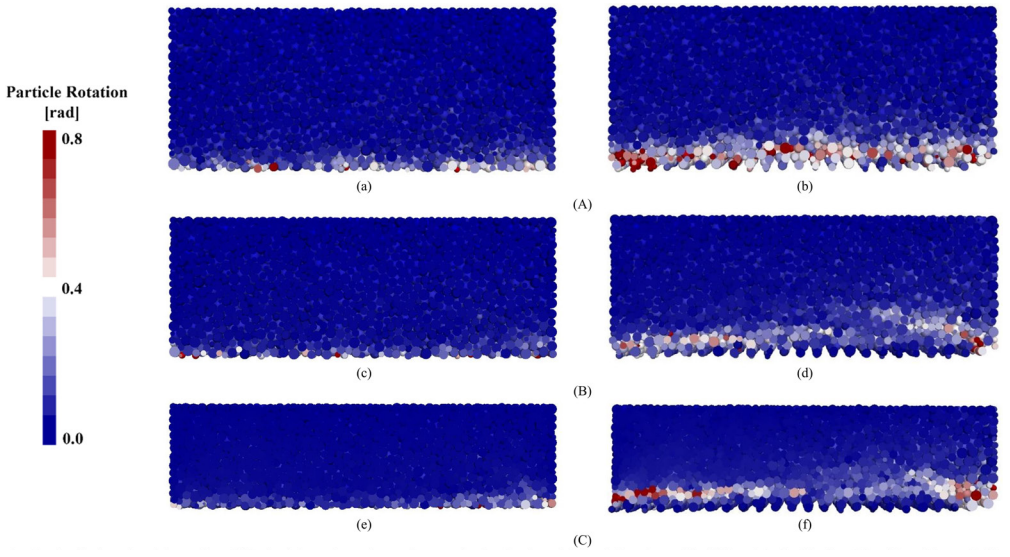

Fig. 19. Distribution of particle rotation within the deformed granular specimen under CV shearing with (a, c, e) $R_n = 0.5$ and (b, d, f) $R_n = 2.0$ after $U_{XB}/h_0 = 0.3$ and for: (A) $p_0 = 100\,\text{kPa}$, (B) $p_0 = 500\,\text{kPa}$ and (C) $p_0 = 1800\,\text{kPa}$.

a constant magnitude at large shearing, which is more evident at higher pressure levels (i.e., $P_0 \geq 500$). Ultimately, the dilation rate becomes negligible, and the volumetric strain-shear displacement curves become almost horizontal, as indicated in Fig. 16(D). As it is expected, however, the values of volumetric strain are zero in CV shearing [14], depicted in Fig. 17(D).

Figures 18 and 19 present the distribution of particle rotation within the deformed granular specimen under CP and CV conditions, respectively. The figures are displayed for different values of wall roughness and pressure level after a horizontal shear displacement of $U_{XB}/h_0 = 0.30$. It is found from the figures that the shearing mechanism of the particulate-wall interface system changes dramatically with the magnitudes of wall roughness and applied pressure level.

It is noteworthy that the width of the wall shear zone in the interface shear test is not uniform along the bottom wall's surface, unlike the lateral infinite shear layer, comparing Figs. 18 and 19 with Figs. 10 and 11. This non-uniformity of the wall shear zone thickness is due to the presence of rigid lateral boundaries of the interface shear box. However, similar to infinite shearing, the width of the wall shear zone achieves its maximum magnitude in the highest wall roughness (i.e., $R_n = 2.0$), Figs. 18(b,d,f) and 19(b,d,f). The width of the localized shear zone is nearly the same in both CP and CV conditions with similar values of wall roughness and pressure level, Figs. 18 and 19. Therefore, the width of the wall shear zone does not depend on the normal confining condition after large shearing as also similarly presented in the FE results.

At lower pressure level (i.e., $p_0 = 100\,\text{kPa}$), the wall shear zone is formed directly at the bottom in the vicinity of the wall surface, Figs. 18(A) and 19(A). This is clearly indicated with higher particle rotations close to the wall surface rather than the rest parts of the specimen. Under both CP and CV shearing conditions, the localized deformation zone moves upward and its distance from the wall surface increases in the higher values of pressure level and wall roughness (i.e., $R_n = 2.0$ and $p_0 = 500$, $R_n = 2.0$ and $1800\,\text{kPa}$). In the mentioned cases, the boundary particles are trapped within the valleys of the wall's surface and the shear zone appears above the surface asperities, Figs. 18(d,f) and 19(d,f). These DEM findings are consistent with those of the Cosserat FE model.

5. Conclusions

According to the performed numerical simulations, the following conclusions can be drawn:

- The progression of deformations exterior to the wall shear zone is more pronounced in CV condition compared to that of CP condition. Although the additional shear deformations out of the wall shear zone are almost negligible in the rough walls under CP, they are continuously developed in

the whole section of the shear layer under CV. Up to a horizontal displacement of $U_{1B}/h_0 = 2.00$ in CV shearing, the localized deformations cannot be detected in the granular medium adjacent to a moving rough wall (e.g., $f_w = 0.05$).

- For interface shearing under CV condition, dilation in the wall shear zone is correspondingly reimbursed by compression within the remaining parts of the granular medium. Thus, the requirement for CV is satisfied within the entire shear layer and the mean value of the void ratio keeps constant across the layer height.
- Comparing the values of the wall friction angle obtained from CP and CV shearing demonstrates that, while more pronounced peaks are distinguished for CP condition, the rather same stationary values are approached for the same interface coefficient, f_w, in both normal confinements. This implies that the peak magnitudes of the wall friction angle are influenced by the stresses induced within the granular body, but the stationary values are independent of the pressure level and the normal confining constraints.
- The localized shear zone has nearly similar width for both CP and CV interface shearing with the same f_w value. It is found that the width of the wall shear zone is independent of the normal confining condition after applying large shear deformations.
- According to the distribution of void ratio and couple stress across the layer height, obtained from the FE analyses, the predicted width of the wall shear zone is about $14d_{50}$ and $15d_{50}$, $9d_{50}$ and $10d_{50}$, $4d_{50}$ and $5d_{50}$ in CP and CV conditions, respectively, for $f_w = 0.10$, 0.25, and 0.50, respectively. The width of the wall shear zone next to a rough wall (e.g., $f_w = 0.05$) under CP shearing is equal to $19d_{50}$, while no localized zone can be distinguished in CV shearing under similar roughness condition.
- The peak and residual stress ratios increase with decreasing pressure level and initial void ratio, and increasing wall roughness. The width of the wall shear zone depends significantly on the initial void ratio and insignificantly on the pressure level. The predicted width of the wall shear zone is larger for higher pressure level and wall roughness, and lower initial void ratio. If the initial void ratio reaches or exceeds the pressure-dependent critical void ratio ($e_0 \geq e_c = 0.84$), then the wall shear zone approaches the size of the granular medium (here, $40 \times d_{50}$). It is revealed that the results of CP interface shearing under higher pressure levels approach those of CV condition.
- The FE results have qualitatively been evaluated against those of DEM simulations in terms of distribution and evolution of field variables within the granular specimen. It is observed that both the microscopic and macroscopic responses of the Cosserat FE model are appropriately in accordance with those of DEM simulations.

Here, however, only qualitative comparisons have been presented between FE and DEM results. In a further article, the new findings of the conducted DEM simulations and the relevant quantitative comparisons are given in more detail.

Acknowledgements

The first author expresses his sincere gratitude and appreciation to the Highest Prestigious Scientific and Professional National Foundation, Iran's National Elites Foundation (INEF) for moral support and encouragement. The authors gratefully acknowledge the handling editor and the anonymous reviewers for their constructive comments and valuable suggestions that helped to improve the quality of the paper.

References

1. J. Tejchman, *FE modeling of shear localization in granular bodies with micro-polar hypoplasticity*, Springer Series in: Geomechanics and Geoengineering, W. Wu, R. Borja [eds.], Springer, Berlin, 2008.
2. J.C. Santamarina, H.S. Shin, *Friction in granular media*, Proceeding of Meso-scale Shear Physics in Earthquake and Landslide Mechanics, Y.H. Hatzor, J. Sulem, I. Vardoulakis [eds.], CRC Press, pp. 157–188, 2009.
3. R. Dyvik, T. Berm, S. Lacasse, B. Raadim, *Comparison of truly undrained and constant volume direct simple shear tests*, Géotechnique, **37**, 1, 310, 1987.
4. D. Negussey, W.K.D. Wijewickreme, Y.P. Vaid, *Constant-volume friction angle of granular materials*, Canadian Geotechnical Journal, **25**, 1, 50–55, 1988.
5. M. Boulon, *Basic features of soil structure interface behavior*, Computers and Geotechnics, **7**, 115–131, 1989.
6. M. Boulon, R. Nova, *Modelling of soil-structure interface behaviour a comparison between elastoplastic and rate type laws*, Computers and Geotechnics, **9**, 1-2, 21–46, 1990.
7. Y. Tsubakihara, H. Kishida, *Frictional behaviour between normally consolidated clay and steel by two direct shear type apparatuses*, Soils and Foundations, **33**, 2, 1–13, 1993.
8. S. Paikowsky, C.M. Player, P.J. Connors, *A dual interface apparatus for testing unrestricted friction of soil along solid surfaces*, ASTM Geotechnical Testing Journal, **18**, 2, 168–193, 1995.
9. T.D. Stark, I.A. Contreras, *Constant volume ring shear apparatus*, ASTM Geotechnical Testing Journal, **19**, 1, 3–11, 1996.
10. E. Evgin, K. Fakharian, *Effect of stress paths on the behaviour of sand steel interfaces*, Canadian Geotechnical Journal, **33**, 6, 853–865, 1996.
11. K. Fakharian, E. Evgin, *An automated apparatus for three-dimensional monotonic and cyclic testing of interfaces*, ASTM Geotechnical Testing Journal, **19**, 1, 22–31, 1996.
12. J. Qiu, F. Tatsuoka, T. Uchimura, *Constant pressure and constant volume direct shear tests on reinforced sand*, Soils and Foundations, **40**, 4, 1–17, 2000.

13. V.K. Garga, J.A. Infante Sedano, *Steady state strength of sands in a constant volume ring shear apparatus*, ASTM Geotechnical Testing Journal, **25**, 4, 414–421, 2002.

14. A. Afzali-Nejad, A. Lashkari, A. Martinez, *Stress-displacement response of sand–geosynthetic interfaces under different volume change boundary conditions*, Journal of Geotechnical and Geoenvironmental Engineering, **147**, 8, 04021062-1.

15. J. Tejchman, *Modelling of shear localisation and autogeneous dynamic effects in granular bodies*, Publication Series of the Institute of Soil and Rock Mechanics, vol. 140, G. Gudehus, O. Natau [eds.], University Karlsruhe, Karlsruhe, Germany, pp. 1–353, 1997.

16. A. Di Donna, A. Ferrari, L. Laloui, *Experimental investigations of the soil-concrete interface: physical mechanisms, cyclic mobilisation and behaviour at different temperatures*, Canadian Geotechnical Journal, **53**, 4, 659–672, 2015.

17. M. Boulon, P. Garnica, P.A. Vermeer, *Soil-structure interaction: FEM computations*, Studies in Applied Mechanics, **42**, 147–171, 1995.

18. V. De Gennaro, P. Lerat, *Soil-structure interface behaviour under cyclic loading*, Proceeding of the Second International Symposium on Pre-failure Deformation Characteristics of Geomaterials, M. Jamiolkowski, R. Lancellotta, D. Lo Pretti [eds.], Torino, Italy, 1999.

19. J. Wang, S. Liu, Y.P. Cheng, *On the role of normal boundary condition in interface shear test for the determination of skin friction along pile shaft*, Canadian Geotechnical Journal, **54**, 9, 1245–1256, 2017.

20. F. Tatsuoka, T. Uchimura, M. Tateyama, *Preloaded and prestressed reinforced soil*, Soils and Foundations, **37**, 3, 79–94, 1997.

21. T. Uchimura, F. Tatsuoka, M. Tateyama, T. Koga, *Behavior of the first prototype and full-scale models of PLPS geosynthetic-reinforced soil structure*, Boston, Annual Convention, ASCE: Geosynthetics in Foundation Reinforcement and Erosion Control Systems, Proceedings of Geo-Congress 98, ASCE, Boston, 34–48, 1998.

22. Y. Yoshimi, T. Kishida, *A ring torsion apparatus for evaluating friction between soil and metal surfaces*, ASTM Geotechnical Testing Journal, **4**, 4, 148–152, 1981.

23. T. Tika-Vassilikos, *Clay-on-steel ring shear tests and their implications for displacement piles*, ASTM Geotechnical Testing Journal, **14**, 4, 457–463, 1991.

24. Y. Tsubakihara, H. Kishida, *Frictional behaviour between normally consolidated clay and steel by two direct shear type apparatuses*, Soils and Foundations, **33**, 2, 1–13, 1993.

25. J. Tejchman, G. Gudehus, *Shearing of a narrow granular layer with polar quantities*, International Journal for Numerical and Analytical Methods in Geomechanics, **76**, 2, 513–536, 2001.

26. T. Ho, R. Jardine, N. Anh-Minh, *Large-displacement interface shear between steel and granular media*, Géotechnique, **61**, 3, 221–234, 2011.

27. H. Liu, E. Song, H.I. Ling, *Constitutive modeling of soil-structure interface through the concept of critical state soil mechanics*, Mechanics Research Communications, **33**, 515–531, 2006.

28. S. Costa D. Aguiar, A. Modaressi-Farahmand-Razavi, J.A. dos Santos, F. Lopez-Caballero, *Elastoplastic constitutive modelling of soil structure interfaces under monotonic and cyclic loading*, Computers and Geotechnics, **38**, 4, 430–447, 2011.

29. W. HUANG, E. BAUER, S.W. SCOTT, *Behavior of interfacial layer along granular soil-structure interfaces*, Structural Engineering and Mechanics, **15**, 3, 315–329, 2003.

30. R. DE BORST, *A generalisation of J2-flow theory for polar continua*, Computer Methods in Applied Mechanics and Engineering, **103**, 347–362, 1993.

31. P. UNTERREINER, I. VARDOULAKIS, M. BOULON, J. SULEM, *Essential features of a Cosserat continuum in interfacial localization*, Proceeding of 3rd International Workshop on Localization and Bifurcation Theory for Soils and Rocks, R. Chambon, J. Desrues, I. Vardoulakis [eds.], Balkema, Rotterdam, 141–155, 1994.

32. J. TEJCHMAN, W. WU, *Numerical Study on Sand and Steel Interfaces*, Mechanics Research Communications, **21**, 2, 109–119, 1994.

33. I. VARDOULAKIS, J. SULEM, *Bifurcation Analysis in Geomechanics*, Blackie Academic & Professional (an imprint of Chapman & Hall): Glasgow, London, U.K., 1995.

34. X.A. LI, H.B. TANG, *A consistent return mapping algorithm for pressure-dependent elastoplastic Cosserat continua and modeling of strain localization*, Computers and Structures, **83**, 1–10, 2005.

35. B. EBRAHIMIAN, A. NOORZAD, M.I. ALSALEH, *Modeling shear localization along granular soil-structure interfaces using elasto-plastic Cosserat continuum*, International Journal of Solids and Structures, **49**, 257–278, 2012.

36. B. EBRAHIMIAN, A. NOORZAD, M.I. ALSALEH, *Modeling interface shear behavior of granular materials using micro-polar continuum approach*, Continuum Mechanics and Thermodynamics, **30**, 1, 95–126, 2018.

37. B. EBRAHIMIAN, A. NOORZAD, M.I. ALSALEH, *A Numerical Study on Interface Shearing of Granular Cosserat Materials*, European Journal of Environmental and Civil Engineering, **30**, 1, 2019, DOI: 10.1080/19648189.2019.1627249.

38. J. TEJCHMAN, E. BAUER, *Numerical simulation of shear band formation with a polar hypoplastic model*, Computers and Geotechnics, **19**, 3, 221–244, 1996.

39. E. BAUER, W. HUANG, *Numerical study of polar effects in shear zone*, Proceeding of 7th International Symposium on Numerical Models in Geomechanics, G.N. Pande, S. Pietruszczak, H. Schweiger [eds.], Balkema, Rotterdam, 133–138, 1999.

40. J. TEJCHMAN, *Behaviour of granular bodies in induced shear zones*, Granular Matter, **212**, 77–96, 2000.

41. W. HUANG, E. BAUER, *Numerical investigations of shear localization in a micro-polar hypoplastic material*, International Journal for Numerical and Analytical Methods in Geomechanics, **27**, 325–352, 2003.

42. E. BAUER, W. HUANG, *Effect of particle rotations on the interface behaviour between a granular layer and parallel rough plates*, Science and Engineering of Composite Materials, **11**, 4, 239–246, 2004.

43. J. TEJCHMAN, W. WU, *FE-investigations of micro-polar boundary conditions along interface between soil and structure*, Granular Matter, **12**, 4, 399–410, 2010.

44. P.V. LADE, R.B. NELSON, *Modeling the elastic behavior of granular materials*, International Journal for Numerical and Analytical Methods in Geomechanics, **11**, 521–542, 1987.

45. M.K. Kim, P.V. Lade, *Single hardening constitutive model for frictional materials*, Computers and Geotechnics, **5**, 307–324, 1988.

46. P.V. Lade, M.K. Kim, *Single hardening plasticity model for frictional materials – II. Yield criterion and plastic work contour*, Computers and Geotechnics, **6**, 13–29, 1988.

47. P.V. Lade, M.K. Kim, *Single hardening plasticity model for frictional materials – III. Comparisons with experimental data*, Computers and Geotechnics, **6**, 31–47, 1988.

48. M.I. Alsaleh, G. Voyiadjis, K. Alshibli, *Modeling strain localization in granular materials using micropolar theory: mathematical formulations*, International Journal for Numerical and Analytical Methods in Geomechanics, **30**, 15, 1501–1524, 2006.

49. K. Alshibli, M.I. Alsaleh, G. Voyiadjis, *Modeling strain localization in granular materials using micropolar theory: numerical implementation and verification*, International Journal for Numerical and Analytical Methods in Geomechanics, **30**, 15, 1525–1544, 2006.

50. A.C. Eringen, *Linear theory of nonlocal microelasticity and dispersion of plane waves*, Letters in Applied and Engineering Sciences, **1**, 2, 129–146, 1973.

51. K. Willam, A. Dietsche, M.M. Iordache, P. Steinmann, *Localization in micropolar continua*, Proceeding of Continuum Models for Materials with Microstructure, H.B. Mühlhaus [ed.], John Wiley and Sons, pp. 297–339, 1995.

52. K.W. Tomantschger, *A boundary value problem in the micropolar theory*, ZAMM – Journal of Applied Mathematics and Mechanics, **82**, 6, 421–422, 2002.

53. H.B. Mühlhaus, *Shear band analysis in granular materials by Cosserat theory*, Ingenieur Archiv., **56**, 389–399, 1986.

54. H.B. Mühlhaus, *Application of Cosserat theory in numerical solutions of limit load problems*, Ingenieur Archiv., 59, 124–137, 1989.

55. ABAQUS, *ABAQUS User's Manual Version 6.3*, Hibbitt, Karlsson and Sorensen Inc.: Pawtucket, RI, USA, 2002.

56. J. Voyiadjis, M.I. Alsaleh, K. Alshibli, *Evolving internal length scales in plastic strain localization for granular materials*, International Journal of Plasticity, **21**, 2000–2024, 2005.

57. M.I. Alsaleh, A. Kitsabunnarat, S. Helwany, *Strain localization and failure load predictions of geosynthetic reinforced soil structures*, Interaction and Multiscale Mechanics, **2**, 3, 235–261, 2009.

58. B. Ebrahimian, A. Noorzad, *Effect of periodic fluctuation of soil particle rotation resistance on interface shear behavior*, IOP Conf. Series: Materials Science and Engineering, 10, 2010, doi:10.1088/1757-899X/10/1/012082.

59. B. Ebrahimian, A. Noorzad, M.I. Alsaleh, *Effects of periodic fluctuations of micropolar boundary conditions on shear localizations in granular soil–structure interaction*, International Journal for Numerical and Analytical Methods in Geomechanics, **36**, 855–880, 2012.

60. B. Ebrahimian, A. Noorzad, *Numerical investigations of shear strain localization in an elasto-plastic Cosserat material*, Proceeding of 18th International Conference on Soil Mechanics and Geotechnical Engineering, Paris, France, 703–706, 2013.

61. B. EBRAHIMIAN, *Numerical investigations of shear banding in granular materials*, Proceeding of 10th HSTAM International Congress on Mechanics, Paper No. 103, Chania, Crete, Greece, 2013.

62. B. EBRAHIMIAN, *Evolution of shear localization in an elasto-plastic cosserat material under shearing*, Key Engineering Materials, **577-578**, 21–24, 2014.

63. B. EBRAHIMIAN, A. NOORZAD, M.I. ALSALEH, *FE simulation of shear localization along granular soil-structure interfaces using micro-polar elasto-plasticity*, Mechanics Research Communications, **39**, 28–34, 2012.

64. J. TEJCHMAN, *Scherzonenbildung und verspannungseffekte in granulaten unter berücksichtigung von korndrehungen*, Publication Series of the Institute of Soil and Rock Mechanics, vol. 140, G. Gudehus, O. Natau [eds.], University Karlsruhe, Karlsruhe, Germany, 1–236, 1989.

65. M. UESUGI, H. KISHIDA, Y. TSUBAKIHARA, *Behavior of sand particles in sand-steel friction*, Soils and Foundations, **28**, 1, 107–118, 1988.

66. J. TEJCHMAN, W. WU, *Experimental and numerical study of sand-steel interfaces*, International Journal for Numerical and Analytical Methods in Geomechanics, **19**, 513–536, 1995.

67. A. GRABOWSKI, M. NITKA, J. TEJCHMAN, *3D DEM simulations of monotonic interface behavior between cohesionless sand and rigid wall of different roughness*, Acta Geotechnica, **16**, 1001–1026, 2021.

68. A. GRABOWSKI, M. NITKA, J. TEJCHMAN, *Comparative 3D DEM simulations of sand–structure interfaces with similarly shaped clumps versus spheres with contact moments*, Acta Geotechnica, 2021, DOI: org/10.1007/s11440-021-01255-0.

69. B. EBRAHIMIAN, E. BAUER, *Numerical simulation of the effect of interface friction of a bounding structure on shear deformation in a granular soil*, International Journal for Numerical and Analytical Methods in Geomechanics, **36**, 2, 1486–1506, 2012.

70. B. EBRAHIMIAN, E. BAUER, *Numerical analysis of interface shear test box size effect on shear behavior of soil specimen using micro-polar continuum approach*, Proceeding of 10th International Workshop on Bifurcation and Degradation in Geomaterials (IWBDG 2014), K. Chau, J. Zhao [eds.], Springer, 143–148, 2015.

71. K.A. ALSHIBLI, S. STURE, *Sand shear band thickness measurements by digital imaging techniques*, Journal of Computing in Civil Engineering, **13**, 2, 103–109, 1999.

72. K.A. ALSHIBLI, S. STURE, *Shear band formation in plane strain experiments of sand*, Journal of Geotechnical and Geoenvironmental Engineering, **126**, 6, 495–503, 2000.

73. I. VARDOULAKIS, K.R. SHAH, P. PAPANASTASIOU, *Modelling of tool-rock shear interfaces using gradient-dependent flow theory of plasticity*, International Journal of Rock Mechanics and Mining Science & Geomechanics Abstracts, **29**, 6, 573–582, 1992.

74. I. VARDOULAKIS, P. UNTERREINER, *Interfacial localisation in simple shear tests on a granular medium modelled as a Cosserat continuum*, Proceeding of Mechanics of Geomaterial Interfaces, A.P.S. Selvadurai, M.J. Boulon (eds.), Elsevier Science B.V., **42**, 487–512, 1995.

75. W. HUANG, S. SLOAN, D. SHENG, *Analysis of plane Couette shear test of granular media in a Cosserat continuum approach*, Mechanics of Materials, **69**, 106–115, 2014.

76. P.A. Cundall, *A discrete numerical model for granular assemblies*, Géotechnique, **29**, 1, 47–65, 1979.

77. J. Wang, M.S. Gutierrez, J.E. Dove, *Numerical studies of shear banding in interface shear tests using a new strain calculation method*, International Journal for Numerical and Analytical Methods in Geomechanics, **31**, 12, 1349–1366, 2007.

78. J. Wang, M. Jiang, *Unifed soil behavior of interface shear test and direct shear test under the influence of lower moving boundaries*, Granular Matter, **13**, 5, 631–641, 2011.

79. W. Huang, L. Huang, D. Sheng, S. Sloan, *DEM modelling of shear localization in a plane Couette shear test of granular materials*, Acta Geotechnica, **10**, 3, 389–397, 2015.

80. A. Martinez, J.D. Frost, *Particle-scale effects on global axial and torsional interface shear behavior*, International Journal for Numerical and Analytical Methods in Geomechanics, **41**, 3, 400–421, 2016.

81. X.Y. Jing, W.H. Zhou, Y. Li, *Interface direct shearing behavior between soil and saw-tooth surfaces by DEM simulation*, Procedia Engineering, **175**, 36–42, 2017.

82. X.Y. Jing, W.H. Zhou, H.X. Zhu, Z.Y. Yin, Y. Li, *Analysis of soil-structural interface behavior using three-dimensional DEM simulations*, International Journal for Numerical and Analytical Methods in Geomechanics, **42**, 2, 339–357, 2018.

83. X. Gu, M. Huang, *Critical state shear behavior of the soil-structure interface determined by discrete element modeling*, Particuology, **35**, 68–77, 2017.

84. H. Zhu, W.H. Zhou, X.Y. Jing, Z.Y. Yin, *Numerical study of the formation of shear bands in soil under interface shearing*, Procedia Engineering, **175**, 102–109, 2017.

85. H.X. Zhu, W.H. Zhou, X.Y. Jing, Z.Y. Yin, *Observations on fabric evolution to a common micromechanical state at the soil-structure interface*, International Journal for Numerical and Analytical Methods in Geomechanics, **43**, 15, 2449–2470, 2019.

86. M. Huang, Y. Chen, X. Gu, *Discrete element modeling of soil-structure interface behavior under cyclic loading*, Computers and Geotechnics, **107**, 14–24, 2019.

87. W.H. Zhou, X.Y. Jing, Z.Y. Yin, X. Geng, *Effects of particle sphericity and initial fabric on the shearing behavior of soil–rough structural interface*, Acta Geotechnica, **14**, 3, 1699–1716, 2019.

88. W.B, Chen, W.H. Zhou, J. Alberto dos Santos, *Analysis of consistent soil–structure interface response in multi–directional shear tests by discrete element modeling*, Transportation Geotechnics, **24**, 100379, 2020.

89. Itasca Consulting Group, *PFC^{3D} – Particle flow code in 3 dimensions user's manual (version 5.0)*, Minneapolis, Minnesota, USA, 2014.

90. W. Ehlers, E. Ramm, S. Diebels, G.A. D'addetta, *From particle ensembles to Cosserat continua: homogenization of contact forces towards stresses and couple stresses*, International Journal of Solids and Structures, **40**, 24, 6681–6702, 2003.

Received December 15, 2020; revised version August 20, 2021.
Published online October 25, 2021.